The Astrophysical Journal, 725:2461–2479, 2010 December 20 doi:10.1088/0004-637X/725/2/2461

THE *SPITZER* c2d SURVEY OF NEARBY DENSE CORES. X. STAR FORMATION IN L673 AND CB188

Anastasia E. Tsitali[1,2], Tyler L. Bourke[1], Dawn E. Peterson[1], Philip C. Myers[1], Michael M. Dunham[3], Neal J. Evans II[3], and Tracy L. Huard[4]
[1] Harvard-Smithsonian Center for Astrophysics, 60 Garden Street, Cambridge, MA 02138, USA; atsitali@cfa.harvard.edu, tbourke@cfa.harvard.edu, dpeterson@cfa.harvard.edu, pmyers@cfa.harvard.edu
[2] School of Physics and Astronomy, University of Southampton, Highfield, Southampton, SO17 1BJ, UK; at306@soton.ac.uk
[3] Department of Astronomy, The University of Texas at Austin, 1 University Station, C1400, Austin, TX 78712-0259, USA; mdunham@astro.as.utexas.edu, nje@astro.as.utexas.edu
[4] University of Maryland, College Park, MD, USA; thuard@astro.umd.edu
Received 2010 May 10; accepted 2010 September 28; published 2010 December 7

ABSTRACT

L673 and CB188 are two low-mass clouds isolated from large star-forming regions that were observed as part of the *Spitzer* Legacy Project "From Molecular Clouds to Planet Forming disks" (c2d). We identified and characterized all the young stellar objects (YSOs) of these two regions and modeled their spectral energy distributions (SEDs) to examine whether their physical properties are consistent with values predicted from the theoretical models and with the YSO properties in the c2d survey of larger clouds. Overall, 30 YSO candidates were identified by the c2d photometric criteria, 27 in L673 and 3 in CB188. We confirm the YSO nature of 29 of them and remove a false Class III candidate in L673. We further present the discovery of two new YSO candidates, one Class 0 and another possible Class I candidate in L673, therefore bringing the total number of YSO candidates to 31. Multiple sites of star formation are present within L673, closely resembling other well-studied c2d clouds containing small groups such as B59 and L1251B, whereas CB188 seems to consist of only one isolated globule-like core. We measure a star formation efficiency (SFE) of 4.6%, which resembles the SFE of the larger c2d clouds. From the SED modeling of our YSO sample we obtain envelope masses for Class I and Flat spectrum sources of 0.01–1.0 $M_{\odot}$. The majority of Class II YSOs show disk accretion rates from 3.3×10^{-10} to 3×10^{-8} $M_{\odot}$ yr^{-1} and disk masses that peak at 10^{-4} to 10^{-3} $M_{\odot}$. Finally, we examined the possibility of thermal fragmentation in L673 as the main star-forming process. We find that the mean density of the regions where significant YSO clustering occurs is of the order of $\sim 10^5$ cm^{-3} using 850 μm observations and measure a Jeans Length that is greater than the near-neighbor YSO separations by approximately a factor of 3–4. We therefore suggest that other processes, such as turbulence and shock waves, may have had a significant effect on the cloud's filamentary structure and YSO clustering.

Key words: ISM: individual objects (L673, CB188) – stars: formation – stars: pre-main sequence – stars: protostars

Online-only material: color figures

1. INTRODUCTION

Observations at infrared wavelengths with the *Spitzer Space Telescope* (hereafter *Spitzer*) enable us to penetrate dense, dusty star-forming regions and obtain a more complete picture of the evolution of protostars and their physical properties. *Spitzer* has a wavelength coverage of 3.6–160 μm and a sensitivity that greatly exceeds that of its predecessors, the *Infrared Astronomical Satellite* (*IRAS*) and the *Infrared Space Observatory*. The lowest luminosity limit that *IRAS* could reach to detect protostars was $L \approx 0.1\ L_{\odot}\ (d/140\ \mathrm{pc})^2$ (Myers et al. 1987), which has improved to $L \approx 4 \times 10^{-3}\ L_{\odot}\ (d/140\ \mathrm{pc})^2$ with *Spitzer* observations (Dunham et al. 2008). This provides us with an essential tool able to detect very low luminosity sources deeply embedded within their cores. The *Spitzer* Legacy Project "From Molecular Clouds to Planet Forming Disks" (hereafter, c2d—Evans et al. 2003) observed five nearby, large molecular clouds and about 100 small, dense cores all within approximately 500 pc. The mid-infrared observations were made with the Infrared Array Camera (IRAC; Fazio et al. 2004) at four bands (3.6 μm, 4.5 μm, 5.8 μm, and 8.0 μm) which are sensitive to dust emission from a young stellar object's (YSO) inner disk, and the Multiband Imaging Photometer (MIPS; Rieke et al. 2004) that traces the disk and envelope emission at 24 μm, 70 μm, and 160 μm. Detections in these bands in conjunction with the near-infrared (NIR; 1–2.5 μm) Two Micron All Sky Survey (2MASS) observations can be used to construct models describing the properties of the central source, the accreting circumstellar disk and its surrounding envelope.

A common way to identify YSOs is through their spectral energy distributions (SEDs) that can be considered to be the characteristic "signatures" of protostars. Due to the significant amount of gas and dust surrounding a YSO, most of the star's radiation is absorbed and reprocessed to longer wavelengths. This excess infrared emission, which stems from the star's disk and envelope, results in SEDs that differ from a simple stellar photosphere spectrum. The shape of the SED can be used to categorize YSOs into groups of different evolutionary stages. The most commonly used classification system is that introduced by Lada (1987), which divides YSOs into three classes depending on the spectral slope of their SED, α, computed for the range from 2 μm to 24 μm, and it is given by

$$\alpha = \frac{d \log[\lambda F(\lambda)]}{d \log \lambda}. \quad (1)$$

According to this system, Class I objects have $0 < \alpha \lesssim 3$, Class II YSOs have $-2 \lesssim \alpha \leqslant 0$, and finally Class III objects correspond to $-3 < \alpha \lesssim -2$. André et al. (1993) suggested the use of Class 0 objects for YSOs more deeply embedded than Class I objects and younger in age. Class 0 objects cannot

be distinguished from Class I objects through their α values, but they can be distinguished empirically with submillimeter data. As they are deeply embedded, their detections are often due to scattered light from their envelope while in several cases they are not detected at all at the shorter infrared wavelengths ($\lambda \lesssim 2$ μm). Greene et al. (1994) updated this classification adding the "Flat Spectrum Sources" in the original system that can be thought of as an intermediate stage between the Class I and Class II phases. This final addition by Greene et al. (1994) led to the final modification of the α value boundaries to $\alpha \geqslant 0.3$ (class I), $-0.3 \leqslant \alpha < 0.3$ (Flat Sources), $-1.6 \leqslant \alpha < -0.3$ (Class II), and $\alpha < -1.6$ (Class III).

This system is regularly thought of as an evolutionary sequence, from the youngest deeply embedded Class 0 protostars, to the oldest Class III YSOs that have accreted most of their envelope mass. The spectral slope α therefore decreases as a YSO evolves, directly reflecting the decrease of the excess infrared emission due to the continuous envelope dissipation (Greene & Lada 1996). However, the shape of the SED and the resulting spectral slope are greatly affected by the inclination of the source, as they are purely observational properties, and one particular YSO could move from one Class to another depending on the viewing angle (Whitney et al. 2003; Dunham et al. 2006; Crapsi et al. 2008). For instance, a Class I source would exhibit a much flatter SED if it were viewed pole-on since its radiation would travel through less opaque medium whereas edge-on inclinations would result in considerable dust and envelope emission. Therefore, a classification system of physical "Stages" was introduced by Robitaille et al. (2006) that directly corresponds to an evolutionary sequence based on the object's physical properties obtained by modeling the SEDs. A Stage 0 object has more than half of its total mass in the envelope and the transition from Stage 0 to I is marked when the system is no longer "envelope dominated." The distinctions between Stages can be determined using the system's envelope accretion rate, disk mass, and stellar mass.

In the following sections, we will attempt to characterize the YSOs not only based on the spectral slope of their SED but also simultaneously using other evolutionary indicators such as the bolometric temperature and the ratio of bolometric to submillimeter luminosity.

2. L673 AND CB188

L673 and CB188 are two small clouds isolated from any large star-forming complexes that were observed as part of the c2d Legacy Project and are located at about 300 $\pm$ 50 pc away (Herbig & Jones 1983). Previous submillimeter observations show that they significantly differ in their star formation activity while the optical images of the two clouds show apparent morphological differences despite their proximity. Studies supporting the previous argument have shown that L673 is filamentary with multiple sites of star formation (e.g., Visser et al. 2002) while CB188 is a small and quiescent globule-like core that harbors a single YSO (e.g., Chen et al. 2007; Kauffmann et al. 2008). A summary of previous studies is presented below.

2.1. Previous Studies

2.1.1. L673

A few studies have been conducted on L673 in the past. Armstrong & Winnewisser (1989) presented CO and ^{13}CO observations of a molecular outflow in L673 and studied its properties in detail. They proposed that the *IRAS* source 19180+1116 is a very likely candidate to be driving the outflow. They measured an outflow mass of 1.6 $M_\odot$ and a physical size of 1.3 pc $\times$ 0.9 pc and also determined its dynamical timescale and kinetic energy. Anglada et al. (1997) used NH_3 observations toward regions with molecular or optical outflows, including L673, and obtained a rotational temperature for L673 $T_{\rm rot} \leqslant$ 12 K. Using the empirical fit of $T_{\rm rot}$ and the kinetic temperature, T_K, from Tafalla et al. (2004), it suggests that $T_K \lesssim 13$ K.

Morata et al. (1997) mapped the CS ($J = 1 \rightarrow 0$) emission in five star-forming regions using the 37 m Haystack Telescope. They used previous observations of the (J, K) = (1, 1) inverse transition of NH_3 of selected sources in L673 to compare them with their C^{34}S ($J = 1 \rightarrow 0$) data and found that their emission peaks show a separation of $\sim$0.2 pc. They located an extended CS emission enhancement with two local maxima associated with the *IRAS* sources 19181+1112 and 19180+1116. This CS emission coincides with the location of the NH_3 condensation that Anglada et al. (1997) detected, which encloses these *IRAS* sources and peaks close to IRAS 19180+1114.

Visser et al. (2002) performed a SCUBA 850 μm survey of many Lynds dark clouds, including L673, to determine their physical properties and identify new protostars and starless cores. They estimate a total mass of 90 $M_\odot$ for L673, a mean column density of 3.4×10^{21} cm^{-2}, and identify a total of eight submillimeter cores, two of them being star forming and the rest starless.

A multitransitional study with BIMA was conducted by Morata et al. (2003) toward a starless core found in L673 at α(J2000) 19$^{\rm h}$20$^{\rm m}$52$^{\rm s}$.1, δ(J2000) 11°15′29″.5, in order to study its structure and chemical evolution using CS, N_2H^+, and HCO^+ observations. The location of this starless core is relatively close to the starless submillimeter core SMM6 that Visser et al. (2002) identified, with a projected angular distance between their centers of $\sim$72″. Their observations of L673 revealed several clumps of size $\leqslant$0.08 pc and showed that the missing flux of the CS ($2 \rightarrow 1$) transition can be accounted for if the cloud is formed by a clumpy and heterogeneous medium. They also measured the abundance ratios for [N_2H^+/CS] and [HCO^+/CS] for selected positions and found that they are in agreement with the predicted values obtained using the chemical model of Taylor et al. (1996, 1998).

Morata et al. (2005) presented combined BIMA and FCRAO maps of the CS core in L673 and found a general filamentary structure connecting several clumps. They estimated their masses and diameters to be in the range of 0.02–0.2 $M_\odot$ and 0.03–0.09 pc, respectively, with the exception of a large 1.2 $M_\odot$ clump. They were also led to the conclusion that the northern and southern regions differ in their chemical composition and structure, with the southern region being more clumpy and less chemically evolved.

2.1.2. CB188

Kandori et al. (2005) used molecular line observations to define the physical properties of 10 Bok globules, including CB188, and also performed Bonnor–Ebert sphere fitting in order to investigate the stability of these globules. The fitting showed that CB188 is gravitationally unstable and using both model and observations they derived a total mass of $\sim$7 $M_\odot$ (compared to the mass $\sim$2.6 $M_\odot$ that Kauffmann et al. 2008 measured) and a central density $n_c \sim 1 \times 10^5$ cm^{-3}. The molecular line observations gave a Local Standard Rest velocity (LSR velocity) of $\sim$7 km s^{-1} for CB188 which is the same as the velocity that

Anglada et al. (1997) measured for L673 from their NH_3 line data.

Chen et al. (2007) performed an interferometric study of the N_2H^+ (1–0) emission for nine low-mass protostellar cores and found faint, extended N_2H^+ emission associated with a Class I object in CB188. They identified the object in CB188 as the *IRAS* source 19179+1129 and measured a bolometric luminosity of 2.6 $L_\odot$ and an envelope mass of 0.7 $M_\odot$. They obtained an LSR velocity of ∼7 km s^{-1} for CB188 and an excitation temperature of 4.6 K from their N_2H^+ (1–0) spectral fitting. The mean density that they derived for the core is $\sim 2 \times 10^6$ cm^{-3}.

Kauffmann et al. (2008) studied the structure and core properties of nearby c2d cores using maps of the thermal dust continuum emission at 1.2 mm and derived a total mass for CB188 of ∼2.6 $M_\odot$, with an effective radius at the 70% peak intensity level of ∼3300 AU. They also identified a young Class I protostar associated with the *IRAS* source 19179+1129 (same as Chen et al. 2007) and gave values for its bolometric temperature, luminosity, and the ratio of the submillimeter to bolometric luminosity using both *IRAS* and *Spitzer*. Using *Spitzer* data they obtained $T_{\rm bol} \sim 433$ K, $L_{\rm bol} \sim 1.1\ L_\odot$, $L_{\rm submm}/L_{\rm bol} \sim 0.025$, and a mass of ∼0.3 $M_\odot$ for the protostar within a peak-centered aperture of 4200 AU.

2.1.3. Physical Association of L673 and CB188

The distance that Kandori et al. (2005) estimate for CB188 from the Bonnor–Ebert sphere fitting as well as from observations (based on their effective temperature, $T_{\rm eff} \sim 19$ K) is approximately 300 pc. Independent studies for both clouds therefore led to the same distance estimates (L673; Herbig & Jones 1983, CB188; Kandori et al. 2005), as well as the same LSR velocities (L673; Anglada et al. 1997, CB188; Kandori et al. 2005; Chen et al. 2007). Hence, we assume that L673 and CB188 are physically associated with each other. The projected distance that we measure between the dense core in CB188 and the most northern submillimeter peak in L673 (see Section 4.2 for discussion on the submillimeter peaks) is approximately 1 pc, which supports the previous argument.

3. OBSERVATIONS

L673 and CB188 were observed by IRAC on the *Spitzer Space Telescope* (Fazio et al. 2004) at 3.6 μm, 4.5 μm, 5.8 μm, and 8.0 μm and the MIPS (Rieke et al. 2004) that operates at 24 μm (MIPS 1) and 70 μm (MIPS 2). The observations were performed at two different epochs for the identification and removal of asteroids. The first IRAC epoch for L673 was performed on 2004 April 20 (PID 139, Astronomical Observation Request (AOR) key 5151744) while the second epoch on 2004 April 21 (PID 139, AOR key 5152256). The IRAC bands 1 and 3 have the same field-of-view which differs from that observed by bands 2 and 4. The overlap region of the IRAC 1 & 3 and IRAC 2 & 4 fields as well as MIPS 1 is used for the data analysis. Four 12 s dithers were performed at each position giving a total 48 s exposure time for the pixels. With IRAC, a field of view of 4.′7 × 29.′0 was observed for L673. The two epochs of MIPS observations at 24 and 70 μm had an integration time of 48 s and 126 s, respectively, and were performed on 2004 April 10 (AOR keys 9414400 and 9424128). The corresponding fields are 17.′0 × 23.′8 for MIPS1 and 12.′7 × 14.′5 for MIPS2.

CB188 was observed with IRAC on 2004 May 25 and 2004 May 26 (PID 139, AOR keys 5150720 & 5151232) with a field of view of 5.′0 × 5.′6. The two epochs of observations for MIPS1 & 2 were performed on 2004 April 10 (AOR keys 9427968 and 9436928), and the fields with MIPS at 24 and 70 μm are 7.′5 × 10.′7 and 4.′7 × 9.′8 respectively.

The IRAC and MIPS images were processed by the Spitzer Science Center (SSC) using the standard pipeline S13 in order to produce Basic Calibrated Images. These images were further processed by the c2d team for the removal of artifacts and quality improvement. Mosaics of the IRAC and MIPS images were then produced using the SSC's software MOPEX and photometry was performed on the extracted sources with a modified version of DOPHOT (Schechter et al. 1993). The 2MASS fluxes of the extracted sources were also included in the catalogs when found, and both images and catalogs were then delivered to the SSC Data Archive. More details about the quality improvement of the images and the production of the mosaics can be found in the c2d data delivery documentation (Evans et al. 2007) and in Harvey et al. (2006).

We also include dust continuum observations at 450 and 850 μm of L673 from Visser et al. (2002), obtained from the SCUBA archive (di Francesco et al. 2008), and at 1.2 mm of CB188 from Kauffmann et al. (2008). As discussed in Section 2.1.3, we will refer to L673 and CB188 as one cloud due to their proximity and assume the same distance of 300 ± 50 pc.

3.1. Identification of YSO Candidates

The main feature that differentiates most YSOs from other sources is the presence of excess emission at infrared wavelengths (near-infrared to far-infrared) compared to a stellar photosphere spectrum. The exception are Class III YSOs without disks that cannot be selected in this way. One way to identify such objects over large fields is through X-ray observations, which are beyond the scope of this paper. Sources classified as "stars" by c2d have fluxes that can be fitted well by a reddened stellar photosphere in at least three bands, while YSO candidates, "YSOc," have detections in all four IRAC bands as well as MIPS1 with S/N > 3. Background galaxies or asymptotic giant branch stars have colors very similar to YSOs and can easily be misclassified as protostars and contaminate the sample.

Color–magnitude and color–color plots were constructed by the c2d team in order to exclude such contaminants. These diagrams combine the Spitzer Wide-Area Infrared Extragalactic Survey (SWIRE) data for each region, which only include stars and galaxies (Lonsdale et al. 2003), in order to eliminate these sources from the catalogs and discriminate between real and "false" YSO candidates. Briefly, the procedure for the YSO selection is based on the construction of probability functions for each of the color–magnitude diagrams that are then multiplied and modified using other photometric properties of the sources. The combined probability function for all the diagrams was chosen so that it eliminates most of SWIRE objects, while at the same time it maximizes the number of YSOs that were selected in Serpens (Harvey et al. 2007) after visual inspection of all candidates to ensure that there are no obvious extragalactic sources. More details about the color–magnitude criteria and construction of the probability functions can be found in Harvey et al. (2007) and Harvey et al. (2006).

From the 27 YSO candidates selected in L673, 5 have an extended morphology while all 3 YSOc detected in CB188 are point sources. Sources are more likely to be extragalactic if they have an extended structure at 3.6 or 4.5 μm, where the sensitivity of the observations is the greatest (Harvey et al. 2007). Figure 1

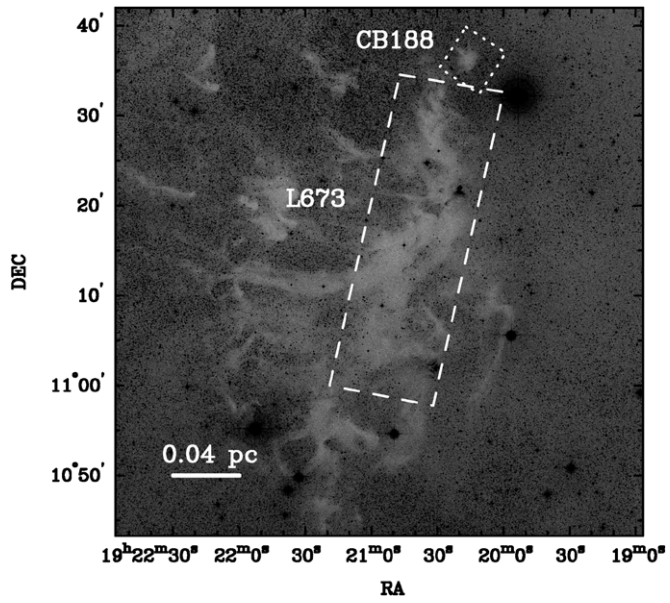

Figure 1. L673 and CB188 in the optical in inverse gray scale (*DSS*). The dashed lines show the area of L673 and the dotted lines show the area of CB188 that was mapped by *Spitzer* with IRAC and correspond to an IRAC field of 4.′7 × 29.′0 and 5.′0 × 5.′6, respectively.

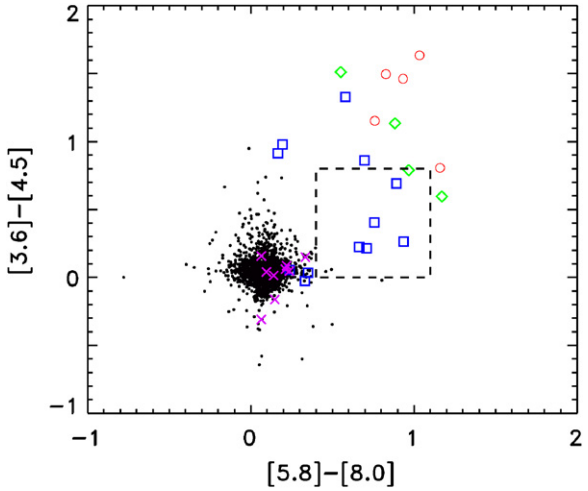

Figure 2. Color–color diagram of the four IRAC bands for all "YSOc" and "stars" in L673 and CB188. Class I, Flat, Class II, and Class III sources were plotted as red (circle), green (diamond), blue (square), and purple (cross). All stars are shown in black (circles). The area defined by the box indicates the location with Class II sources, identified by Allen et al. (2004).

(A color version of this figure is available in the online journal.)

illustrates the area of L673 and CB188 mapped with IRAC, overlaid on a *Digital Sky Survey* (*DSS*) optical image. Overall 30 YSO candidates were extracted from the catalogs for L673 and CB188, whose coordinates and Class type are given in Tables 1 and 2, while their photometric properties can be found in Tables 3 and 4.

4. RESULTS

4.1. YSO Candidates in L673 and CB188

Out of the 30 YSO candidates, 27 belong to L673 and 3 to CB188. Based on the spectral SED slopes (α) of our YSOc sample we find five Class I SEDs, four Flat SEDs, twelve Class II SEDs, and nine Class III SEDs, with corresponding percentages of 16.6% (±7.5),13.3% (±6.6), 40% (±11.5), and 30% (±10).

Table 1
YSOs in L673

YSOs	Class	R.A. (J2000)	Decl.(J2000)
1	I	19:20:13.903	+11:19:55.91
2	II	19:20:13.942	+11:19:53.30
3	II	19:20:19.490	+11:21:54.47
4	II	19:20:19.536	+11:22:51.13
5	II	19:20:21.042	+11:19:20.04
6	Flat	19:20:24.123	+11:22:17.75
7	III	19:20:24.179	+11:17:33.52
8	II	19:20:24.756	+11:22:34.87
9	I	19:20:25.311	+11:22:17.28
10	I	19:20:25.856	+11:19:53.71
11	Flat	19:20:25.921	+11:22:21.11
12	II	19:20:25.968	+11:20:08.27
13	Flat	19:20:26.037	+11:19:52.29
14	II	19:20:26.166	+11:19:49.21
15	II	19:20:26.720	+11:19:55.56
16	III	19:20:29.373	+11:17:02.00
17	II	19:20:30.850	+11:17:54.93
18	III	19:20:34.404	+11:14:21.25
19	III	19:20:38.416	+11:25:15.56
20	III	19:20:44.289	+11:15:18.24
21	II	19:20:45.720	+11:23:53.87
22	III	19:20:56.652	+11:07:58.68
23	III	19:20:15.802	+11:22:19.85
24	II	19:20:16.566	+11:22:33.96
25	II	19:20:16.829	+11:17:43.24
26	I	19:20:24.661	+11:22:17.50
27	I	19:20:27.044	+11:20:11.43

Table 2
YSOs in CB188

YSOs	Class	R.A. (J2000)	Decl. (J2000)
1	III	19:20:10.627	+11:36:59.50
2	III	19:20:12.547	+11:37:48.09
3	Flat	19:20:14.902	+11:35:40.45

In comparison, Evans et al. (2009) measured percentages of 14%, 9%, 64%, and 13% for all of the 1024 YSOc included in the c2d sample. This implies that L673 and CB188 are probably neither extremely young or old, compared to the ensemble of the five clouds studied by Evans et al. (2009). We note that our sample is not complete in Class III YSOs and we cannot accurately determine a lower mass limit for the completeness. However, this does not affect the conclusions presented in this work.

IRAC photometry can also be used to discriminate between sources of different evolutionary stages. A color–color diagram constructed using IRAC fluxes is shown in Figure 2, with the YSO candidates color coded according to their Lada class type. The box indicates the location identified by Allen et al. (2004) where most Class II objects are expected to be found, while the more embedded Class I and Flat spectrum sources are expected to lie above and to the right of the box. On the other hand, Class III sources have colors similar to stars and other information is needed to confirm their nature, such as elevated X-ray emission or spectral signatures of accretion. This elevated X-ray emission arises due to the enhanced magnetic activity in their chromospheres relative to main-sequence stars (Feigelson & Montmerle 1999). A three-color image of L673 is presented in Figure 3 and its YSO distribution in Figure 4. Similarly, the YSO distribution for CB188 is illustrated in Figures 5 and 6.

Table 3
Photometry Of YSO Candidates in L673

Source	J (mJy)	H (mJy)	K_s (mJy)	3.6 (mJy)	4.5 (mJy)	5.8 (mJy)	8.0 (mJy)	24 (mJy)	70 (mJy)
1	0	0	0	3.65 ± 0.205	4.96 ± 0.283	5.81 ± 0.29	9.15 ± 0.454	65.6 ± 6.07	
2	4.84 ± 0.156	6.33 ± 0.239	5.95 ± 0.239	4.05 ± 0.232	3.34 ± 0.210	2.84 ± 0.19	3.64 ± 0.296	22.5 ± 3.11	
3	153 ± 3.66	343 ± 14.2	489 ± 10.8	614 ± 34.6	576 ± 31.8	536 ± 26.2	583 ± 28.5	724 ± 67.1	
4	11.1 ± 0.236	18.9 ± 0.471	18.8 ± 0.451	11.4 ± 0.574	8.98 ± 0.44	8.04 ± 0.39	8.37 ± 0.401	7.02 ± 0.687	
5	3.95 ± 0.0981	68.8 ± 1.58	247 ± 4.79	306 ± 18.1	204 ± 10.7	206 ± 10.1	154 ± 7.31	93.1 ± 8.62	
6	0.152	0.751 ± 0.0809	8.27 ± 0.312	15. 9 ± 0.869	41.4 ± 3.13	60.8 ± 2.94	54.7 ± 2.66	101 ± 11.2	
7	0.368 ± 0.0423	10.6 ± 0.264	44.8 ± 0.95	53.1 ± 2.65	39.7 ± 1.96	34.8 ± 1.65	20 ± 0.957	1.74 ± 0.215	
8	0.0577	0.483	1.45 ± 0.102	4.14 ± 0.21	5.92 ± 0.299	6.93 ± 0.35	7.13 ± 0.362	5.91 ± 0.697	
9	0	0	0	2.68 ± 0.382	7.81 ± 0.524	18.6 ± 0.921	26.1 ± 1.26	395 ± 37.6	
10	0	0	0	15.3 ± 1.03	28.6 ± 1.47	44.5 ± 2.23	48.5 ± 2.41	1060 ± 98.6	2960 ± 277
11	0.0456	3.99 ± 0.136	11.1 ± 0.297	18.4 ± 1.02	20.6 ± 1.09	24.5 ± 1.21	39 ± 1.88	207 ± 19.4	
12	0.354	0.262	0.667 ± 0.0792	7.72 ± 0.404	12.3 ± 0.6	13.6 ± 0.661	8.8 ± 0.473	(2.18 ± 0.462)	
13	0.622	2.2 ± 0.208	10.8 ± 0.647	32.2 ± 1.63	59.2 ± 2.89	80 ± 3.83	97.7 ± 4.79	148 ± 19.6	
14	0.267	1.07 ± 0.0917	5.66 ± 0.235	8.31 ± 0.443	6.61 ± 0.357	5.48 ± 0.4	5.47 ± 0.715	(27.6 ± 5.4)	
15	0.0671	0.115	1.76 ± 0.0777	14.2 ± 0.765	21.3 ± 1.09	23.3 ± 1.15	14.7 ± 0.727	(5.61 ± 1.38)	
16	0.174	76.1 ± 1.68	181 ± 3.49	164 ± 8.66	110 ± 5.47	102 ± 4.88	60.3 ± 2.93	18.5 ± 1.71	
17	12.9 ± 0.286	32.3 ± 0.744	49.5 ± 1.05	61 ± 3.07	74.6 ± 3.74	78.9 ± 3.77	97.2 ± 4.63	247 ± 22.8	350 ± 35
18	29.2 ± 0.699	135 ± 3.11	230 ± 4.88	190 ± 10.2	133 ± 6.66	115 ± 5.54	76.2 ± 3.67	30.4 ± 2.82	
19	13.4 ± 0.32	107 ± 2.45	224 ± 5.16	213 ± 11.3	158 ± 8.24	144 ± 7.0	106 ± 5.0	54.8 ± 5.13	
20	5.07 ± 0.103	66.4 ± 1.47	200 ± 3.68	203 ± 11.9	133 ± 6.97	128 ± 6.21	78.8 ± 3.75	25.4 ± 2.35	
21	43.4 ± 0.96	301 ± 15.3	1000 ± 26.7	1310 ± 144	2880 ± 193.0	3240 ± 168	2990 ± 172	755 ± 70.2	
22	183 ± 4.05	749 ± 21.4	1200 ± 22.1	838 ± 54.9	566 ± 32.6	523 ± 26	352 ± 16.8	178 ± 16.5	
23	83.6 ± 1.62	338 ± 8.09	541 ± 14.5	404 ± 22.9	225 ± 16.3	213 ± 10.6	132 ± 6.37	43.2 ± 4.04	
24	13.1 ± 0.241	122 ± 2.69	339 ± 6.56	441 ± 24.1	300 ± 20.2	313 ± 16.7	211 ± 10.2	118 ± 11.0	
25	34.6 ± 0.765	190 ± 4.38	369 ± 7.15	347 ± 20.9	219 ± 12.6	223 ± 11.8	164 ± 8.18	136 ± 12.6	
26	0.0614	0.123	4.07 ± 0.191	31.4 ± 1.53	78.1 ± 3.84	122 ± 5.96	156 ± 7.54	722 ± 74.4	
27	0	1.17	4.98 ± 0.252	64.3 ± 3.76	165 ± 9.81	212 ± 11.5	246 ± 11.9	411 ± 38.0	1232 ± 246

Note. Values in parentheses indicate fluxes that were not used for the SEDs and the SED modeling.

Table 4
Photometry Of YSO Candidates in CB188

Source	J (mJy)	H (mJy)	K_s (mJy)	3.6 (mJy)	4.5 (mJy)	5.8 (mJy)	8.0 (mJy)	24 (mJy)	70 (mJy)
1	126 ± 2.44	530 ± 18.6	935 ± 20.7	833 ± 43.3	405 ± 33.1	493 ± 24	283 ± 14.8	90.4 ± 8.33	
2	29.1 ± 0.696	107 ± 2.65	180 ± 3.02	266 ± 14.8	182 ± 13.1	199 ± 9.96	131 ± 6.55	30.1 ± 2.78	
3	6.49 ± 0.191	24.8 ± 0.639	50.4 ± 1.07	65.1 ± 3.16	87.1 ± 4.79	125 ± 5.95	165 ± 8.32	843 ± 77.7	1980 ± 184

Most of the Class I and Flat sources are closely spaced (77.7% or seven out of nine) in regions of high A_v showing that they must be relatively young objects, still located at their birthplace. Such distribution is indicative of the core's primordial structure as most of the youngest YSOs are expected to be concentrated in the densest, highly extinguished regions (Gutermuth et al. 2009). The Class II and III SEDs are more evenly distributed but still follow the general structure of the thin, dense filaments of L673.

4.2. Submillimeter Peaks in L673

We obtained 450 μm and 850 μm submillimeter data for L673 from the literature (Visser et al. 2002; di Francesco et al. 2008) and we inspected the submillimeter peaks at 850 μm in order to identify any associated YSOs within 15″ of the peak which is the beam size of the 850 μm observations. The coordinates of all the submillimeter peaks from Visser et al. (2002) are given in Table 5 while Figure 7 locates the peaks against the 8.0 μm background. Two of the peaks are associated with the Class I/Flat groups, namely SMM1 and SMM2 (see Figures 8 and 9—we will use the names for the submm peaks given by Visser et al. 2002 to avoid confusion). As Figure 10 shows, SMM1 is associated with two Flat (source IDs 6 and 11) and two Class I sources (source IDs 9 and 26) that form a straight line in projection. This line seems to be perpendicular to the overall elongation of the filament, and the sources also seem to be equally spaced with surprisingly small angular separations. Implications of this alignment and separations will be discussed later in Section 4.11. The 850 μm emission peak SMM1 is specifically centered at a Class I YSO (source ID 9) with a bipolar outflow. The scattered light stemming from the envelope cavity of this YSO becomes remarkably clear at the IRAC 1 and 2 bands since at 4.5 μm high-velocity shocked outflows can be detected via the H_2 emission line feature that lies within this band (Noriega-Crespo et al. 2004; Jørgensen et al. 2006).

The other submillimeter peak, SMM2, lies to the south of SMM1 and is associated with a group of six YSOs; two Class Is, one Flat source, and three Class IIs. The peak has a more extended morphology and it is almost impossible to distinguish which YSO contributes the most to the overall flux of the peak. The YSOs with source IDs 14 (Class II), 13 (Flat), and 10 (Class I) are aligned and overlap at longer wavelengths (no resolved separation at 24 μm and 70 μm).

The rest of the submillimeter peaks at 450 μm and 850 μm seem to pinpoint the starless cores of this region,

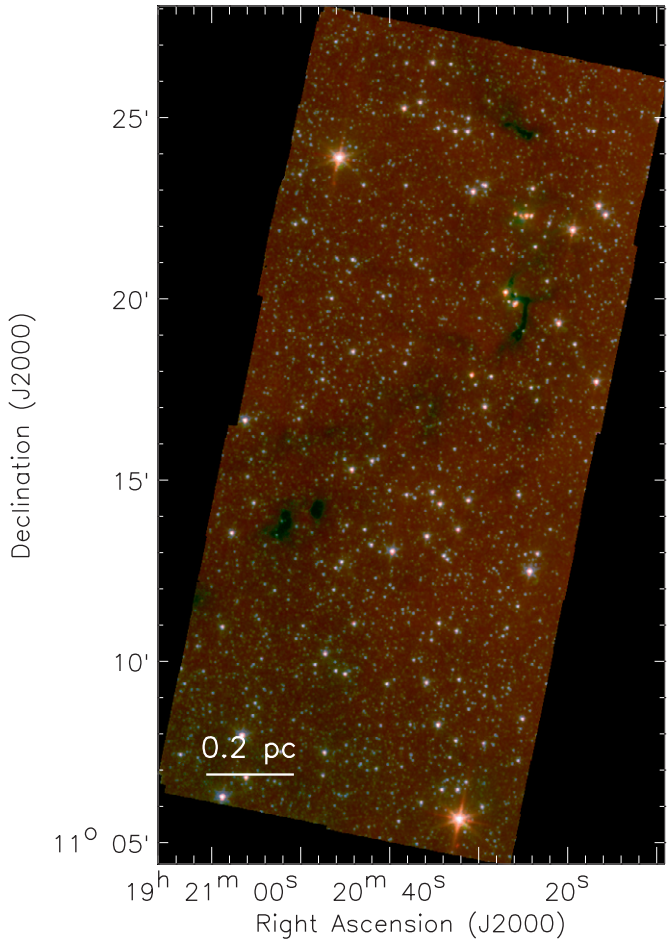

Figure 3. Three-color composite image of L673: red (8.0 μm), green (4.5 μm), and blue (3.6 μm).

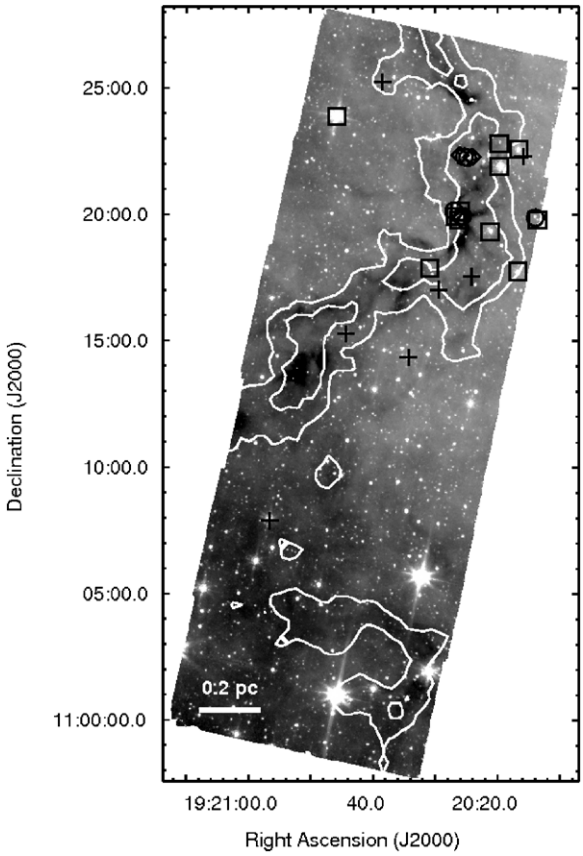

Figure 4. YSO population in L673 overlaid on the 8.0 μm *Spitzer* image. Class I, Flat, Class II and Class III sources correspond to the symbols circle, diamond, box, and cross point, respectively. The $A_V = 10$ and $A_V = 14$ contours from an extinction map created by 2MASS data are also shown.

namely SMM3, SMM4, SMM5, SMM6, SMM7, and SMM8 (SMM3 and SMM5 are shown in Figure 11). However, after careful inspection of the images we identified a source in SMM4 which is associated with dense gas as seen in the 8.0 μm image (R.A. $19^h20^m24\overset{s}{.}77$, decl. 11°24′28 53″) and is also visible at 24 μm (Figure 12). The model SED of this source is shown in Section 4.8, Figure 19. As the SED is not well sampled for wavelengths greater than 24 μm, further observations are needed to determine whether this source is a YS0. In order to determine more of the source's properties, we calculated its bolometric temperature and luminosity. The method for these calculations is described in Section 4.6. We find a bolometric luminosity of 0.002 $L_\odot$ and bolometric temperature of 372 K which places it in the Class I range (refer to Section 4.6 for $T_{\rm bol}$ ranges) and also agrees with the classification based on the spectral slope of its SED, with an $\alpha = 1.14$. However, the lack of SED information is probably responsible for the low bolometric luminosity derived. The resolution of the submillimeter observations is 19″ while the source's distance from the submillimeter peak is less than 6″. Therefore, it is possible that the submillimeter emission is due to the presence of this embedded object.

4.3. A Class 0 Candidate in L673

Right above the Class I source 27, at the northern edge of SMM2, lies a source that is deeply embedded (as seen at 8.0 μm and also confirmed by Dunham et al. 2008) and increases in flux density from 5.8 to 70 μm. This source, located at R.A. $19^h20^m26\overset{s}{.}54$, decl. 11°20′25 86″, is classified as a "red" source in the c2d catalog with an α of 0.74. Its flux at 24 μm is three times larger than the flux at 5.8 μm but is below the detection limit at 8.0 μm, and was therefore not classified as a YSO candidate (one of the criteria for YSO selection is the detection of a source in all four IRAC bands as well as MIPS1 band). Observations at 350 μm using SHARC-II on the Caltech Submillimeter Observatory (CSO) were obtained for the Class 0 candidate (M. M. Dunham et al. 2010, in preparation). As Figure 13 shows, this source occupies the peak of both the 70 μm and 350 μm emission. We believe that this source is in fact a Class 0 candidate as calculations of $T_{\rm bol}$ in Section 4.6 yield a bolometric temperature of 33 K, and the model SED of this source in Section 4.9 shows a significant amount of far-infrared emission relative to the mid-infrared, as expected for deeply embedded protostars.

4.4. Upper Limits

Unfortunately, not all of the YSO candidates had 70 μm coverage and many others had no 70 μm detections. The YSOc that were not covered by the 70 μm observations have the following source IDs: 3, 4, 6, 8, 9, 11, 21, 22, 23, 24, and 26. Only three of our YSO candidates had 70 μm detections (IDs 10, 17 & 27) and we therefore obtained upper limits for the rest of the Class I, II, and Flat Spectrum Sources using aperture photometry. The upper limits for the Class III objects in our sample cannot be determined as they have no detections at 70 μm thus indicating that they have accreted most of their

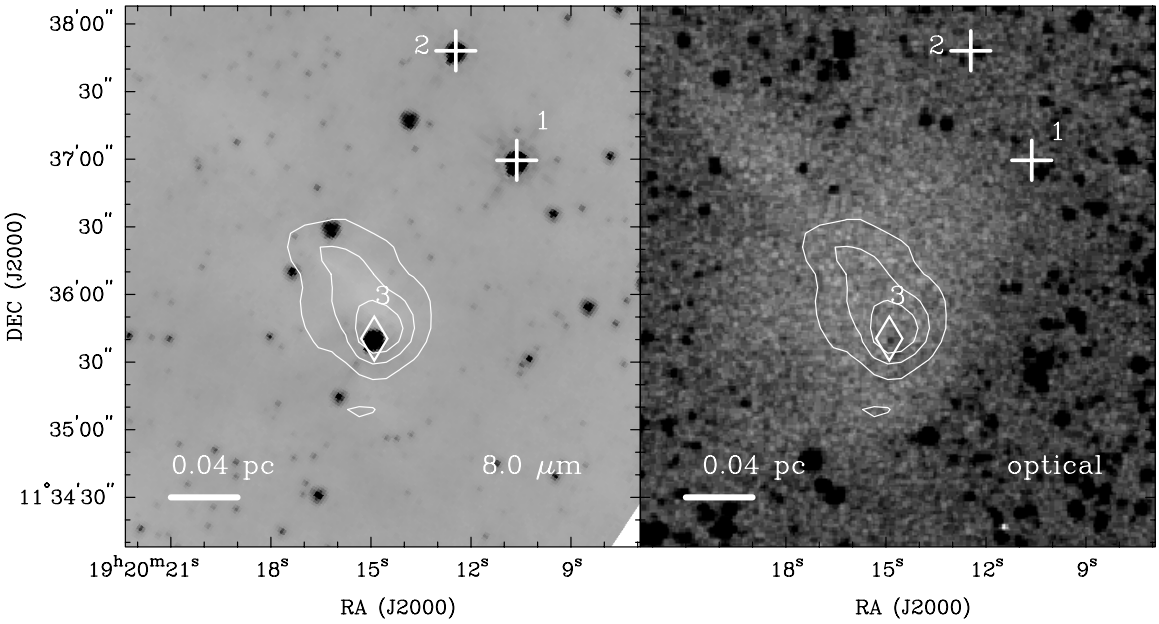

Figure 5. YSO population in CB188 is shown in inverse gray scale 8.0 μm *Spitzer* image (left) and in the optical (right), with the 850 μm data shown as contours. The 850 μm contour levels begin at 4σ and increase by 2σ ($\sigma = 2.8 \times 10^{-2}$ Jy beam^{-1}; Visser et al. 2002). The symbols diamond and cross correspond to the Flat and Class III sources, respectively.

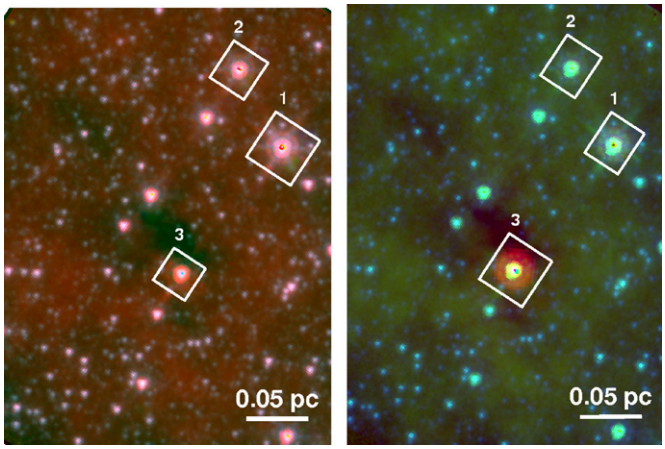

Figure 6. Three-color composite images showing the YSO population in CB188. Left: the IRAC bands 3.6 μm, 4.5 μm, and 8.0 μm are represented as blue, green, and red (north is up and east is left). Right: the IRAC bands 3.6 μm and 8.0 μm are shown as blue and green while the MIPS band 24 μm is shown in red. The Flat Spectrum Source 3 is located right next to the dark core.

envelope mass. We calculated the upper limits individually for each source as most of them constitute confused regions containing many unresolved YSO candidates. Unfortunately, SMM1 was not observed at 70 μm and therefore we could not constrain the fluxes of the YSOc at this wavelength.

We used the flux of SMM2 at 450 μm and 850 μm by Visser et al. (2002) as an upper limit for all of the associated YSOc. The SMM1 peak is clearly centered at the Class I outflow source and we therefore assumed that the 850 and 450 μm flux is due to this YSO. As far as the other YSO candidates at SMM1 are concerned, we obtained limits for each one of them individually using aperture photometry. For sources that have no direct association with the dust emission at 850 μm we used the minimum map rms of 0.04 Jy/beam (di Francesco et al. 2008) as a limit. Finally, observations at 350 μm using SHARC-II on the CSO were obtained for both SMM1 & SMM2 and the

Table 5
Coordinates of Submillimeter Sources[a] in L673

Name	R.A. (J2000)	Decl. (J2000)
SMM1	19:20:25.205	+11:22:16.63
SMM2	19:20:25.848	+11:20:02.67
SMM3	19:20:47.966	+11:14:12.18
SMM4	19:20:24.662	+11:24:33.59
SMM5	19:20:51.676	+11:13:44.43
SMM6	19:20:48.132	+11:16:00.19
SMM7	19:20:23.094	+11:22:49.48
SMM8	19:21:02.618	+11:11:46.18

Note. [a] From Visser et al. (2002).

Class 0 candidate (M. M. Dunham et al. 2010, in preparation). The 350 μm detections for SMM1 and SMM2 correspond to the YSO candidates that occupy the center of these peaks (YSOc 9 in SMM1, YSOc 10 & 13 in SMM2) and they were included in the SEDs for later modeling in Section 4.8.

Some of the 70 μm upper limits of the Class II sources (IDs: 12, 14, and 15) were not used in later modeling. After careful inspection of the images we concluded that these YSOs have no real detections at 24 μm and contamination from the nearby bright Class I and Flat sources resulted in band-filled fluxes at this wavelength that were not valid. A band-filled flux is obtained by fitting a point-spread function (PSF) profile at the source's exact location at bands where the source was not found in the original extraction process. Invalid fluxes may arise especially at longer wavelengths when a much broader PSF is applied in crowded regions. In this case, the wings of a nearby bright source can be detected, resulting in a false flux. We therefore did not include the 24 μm fluxes of these three sources in the SED modeling.

4.5. The SEDs

SEDs were constructed for all Class I, Flat, II and III sources in L673 and CB188 using the same method as Harvey et al.

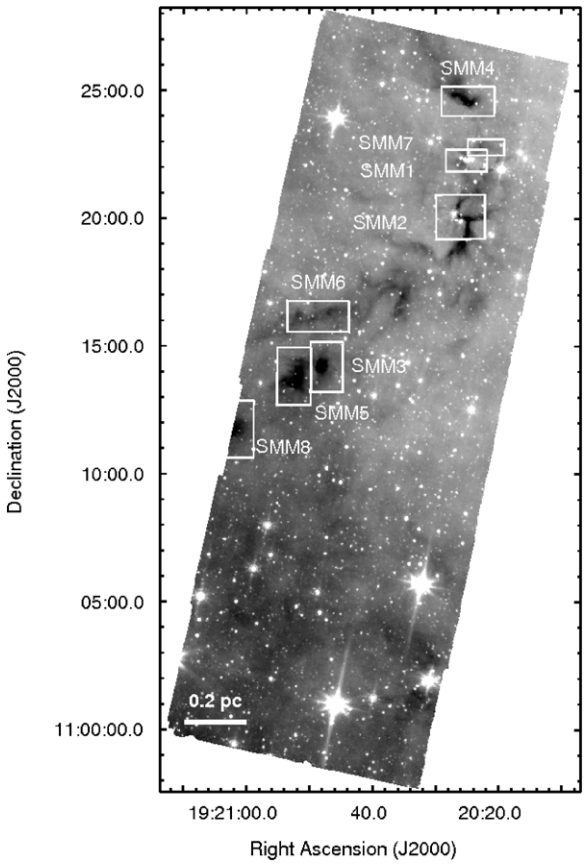

Figure 7. Locations of the submillimeter peaks SMM1-SMM8 (Visser et al. 2002) in L673, overlaid on the 8.0 μm *Spitzer* image. The peaks SMM3, SMM5, SMM6, SMM7, and SMM8 appear to be starless.

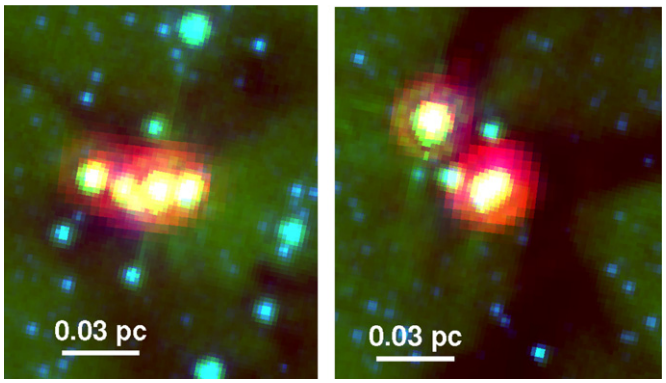

Figure 9. Three-color composite image of SMM1 and SMM2: red (24 μm), green (8.0 μm), and blue (3.6 μm). Left: four YSOs associated with the 850 μm submillimeter peak SMM1. Right: YSOs associated with the submillimeter peak SMM2. North is up and east is left.

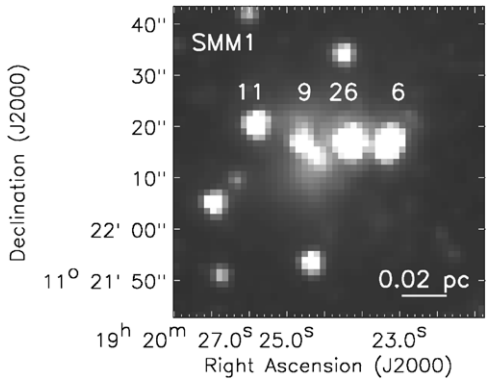

Figure 10. Group of four YSOs associated with SMM1 at 4.5 μm. Source Classes: 11 (Flat), 9 (Class I), 26 (Class I), 6 (Flat).

(2007), and are shown in Figures 14 and 15. The observed fluxes are dereddened using the interstellar extinction law of Weingartner & Draine (2001) with $R_V = 5.5$ and the dereddened SEDs are then fitted to the model of a K7 photosphere. The median SED for T Tauri stars in Taurus is also shown (derived from D'alessio et al. 1999) and is normalized to the optical dereddened fluxes of the YSOs. We use the median SED from D'Alessio et al. (1999) in order to be consistent with the previous c2d papers that use this method (e.g., Harvey et al. 2007).

According to the classification scheme of Harvey et al. (2007) and Merín et al. (2008), the Class II YSOs can be categorized depending on the shape of their SED compared to the median SED of Taurus. A system could therefore be "T-type" corresponding to a SED that follows closely the

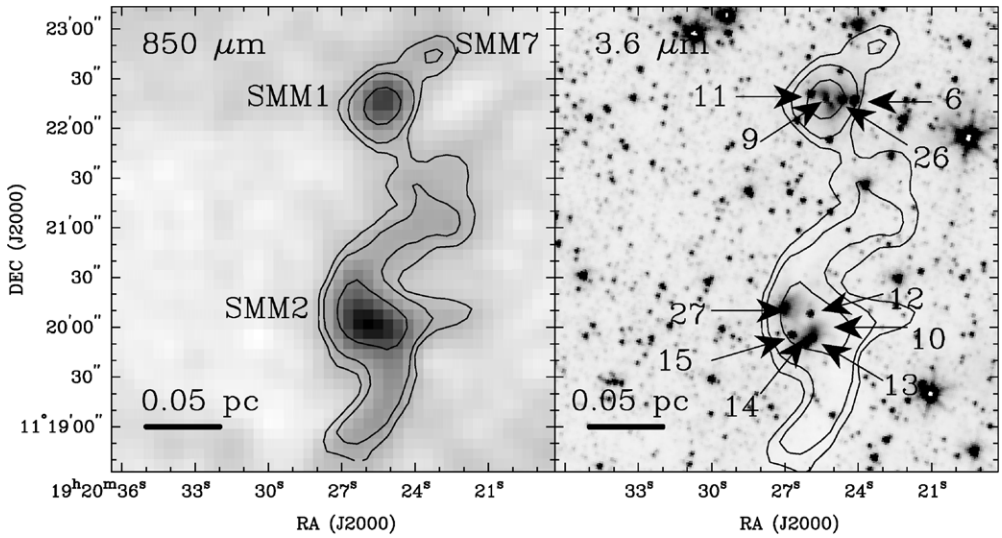

Figure 8. Submillimeter peaks SMM1, SMM2, and SMM7 from Visser et al. (2002) with associated YSOs and 850 μm contours at 3σ, 5σ, 12σ with σ 28 mJy beam^{-1}.

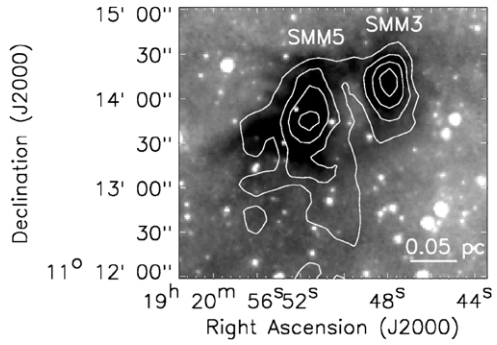

Figure 11. Starless Cores SMM3 and SMM5 at 8.0 μm (gray scale) with the 850 μm data as contours. The contour levels are at 5σ, 7σ, 9σ, and 11σ (σ = 28 mJy beam^{-1}; Visser et al. 2002). The good correspondence between the submillimeter emission and the 8.0 μm absorption is apparent.

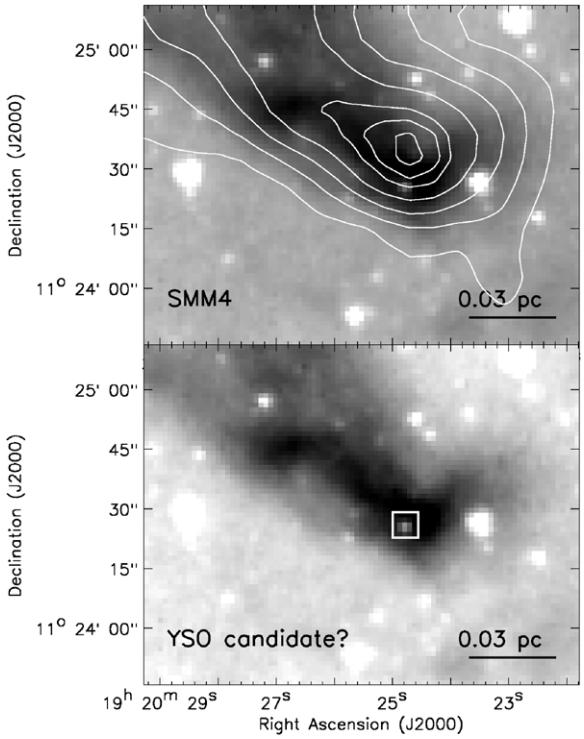

Figure 12. Possible YSO candidate in SMM4 overlaid on the 8.0 μm *Spitzer* image. Top: the 850 μm contours are at 3σ, 5σ, 7σ, 9σ, 11σ,12σ, and 13σ with σ = 28 mJy beam^{-1} (Visser et al. 2002). Bottom: the box indicates the location of the possible YSO candidate.

median, "L-type" for a SED that displays a much smaller infrared excess compared to the median and "H-type" for IR excess that exceeds the median. Different evolutionary processes in the disks such as dust sedimentation, settling, and grain growth can result in flatter L-type structures. These objects have been referred to in the literature as anemic (Lada et al. 2006), evolved (Hernández et al. 2007), and homologously depleted (Currie et al. 2009). An interesting type of system are the "LU" objects which have photospheric fluxes at mid-infrared wavelengths up to 8.0 μm but for wavelengths greater than that they show a sudden jump in their SED almost up to the level of the median SED of Taurus. These strange SED configurations could probably be due to the presence of holes in the inner disks, with planet formation being one of the possible processes responsible for this dust clearance. LU-type objects, which are also called transitional or cold disks (Calvet et al. 2005; Burkert & Hartmann 2004), have been observed in past studies (Harvey et al. 2007; Alcalá et al. 2008; Merín et al. 2008) but are generally quite rare (Muzerolle et al. 2010).

In our SED sample of 12 Class II YSOs, there are 2 H-type objects, 2 T-type, 7 L-type, and 1 LU-type object. However, the LU-nature of YSO number 2 is rather controversial as its 24 μm detection is very likely to be affected by the presence of the Class I protostar (ID 1) which lies less than 6″ away from it. Its "LU" nature should therefore be considered with some doubt. On the same note, there is no apparent point source detection at 24 μm for sources 12, 14, and 15. It seems that the Class II source 14 was band-filled at this wavelength due to contamination from the much brighter Flat spectrum source (YSO ID 13). In addition, even though both sources 12 and 15 exhibit H-Type SEDs this is probably due to the imperfect fitting to the stellar photosphere spectrum, which is a direct result of the lack of short wavelength data (Harvey et al. 2007). Therefore, we do not consider the 24 μm fluxes of YSOs 12, 14, and 15 to be reliable and remove them from the SEDs as well as from the SED modeling (Section 4.8) in order to avoid any confusion. Consequently, their nature still remains uncertain and further observations are needed in order to make any reliable assumptions. Finally, the SED of the "Class III YSO" 7 shows no excess infrared emission, and thus its YSO nature cannot be confirmed. Additional observations, such as X-rays, are needed to draw a conclusion. These four sources (7, 12, 14, and 15) are fitted well by a stellar photosphere spectrum in later modeling, Section 4.8.

4.6. $L_{\rm bol}$, $T_{\rm bol}$ and $L_{\rm bol}/L_{\rm smm}$

The bolometric luminosity and the ratio of $L_{\rm bol}$ to $L_{\rm smm}$ provide us with a way to observationally classify and characterize the YSO candidates along with the spectral slope system. The submillimeter luminosity is the integrated SED for wavelengths $\lambda \geqslant 350$ μm. André et al. (1993) proposed that YSO candidates could be classified as Class 0 as long as the $L_{\rm bol}/L_{\rm smm}$ ratio does not exceed the value 200. They argued that this empirical value marks the stage of the YSO at which half of the system's total mass is included in the envelope and any values greater than this number correspond to decreasing values of envelope mass. It is an essential tool for identifying a YSO's evolutionary status as it is less affected by geometry (Young & Evans 2005; Crapsi et al. 2008). Myers & Ladd (1993) and Chen et al. (1995) on the other hand suggested that specific ranges for the bolometric temperature, a measure of the flux-weighted mean frequency of the input SED, could be used as indicators of the spectral Class of the YSOs. They proposed ranges of

1. $T_{\rm bol} < 70$ K for Class 0 objects;
2. 70 K $\leqslant T_{\rm bol} \leqslant$ 650 K for Class Is; and
3. 650 K $< T_{\rm bol} \leqslant$ 2800 K for Class IIs.

These limits do not take into account Class III objects, and the spectral slope of the SED is used to distinguish them from Class IIs instead. The bolometric luminosity is computed by integrating over the entire SED while $T_{\rm bol}$ is a measure of the flux-weighted mean frequency of the input SED as mentioned above. $L_{\rm bol}$, $T_{\rm bol}$, and $L_{\rm smm}$ were measured using the method of Dunham et al. (2008) using the following relations,

$$L_{\rm bol} = 4\pi d^2 \int_0^\infty S_\nu d\nu, \quad (2)$$

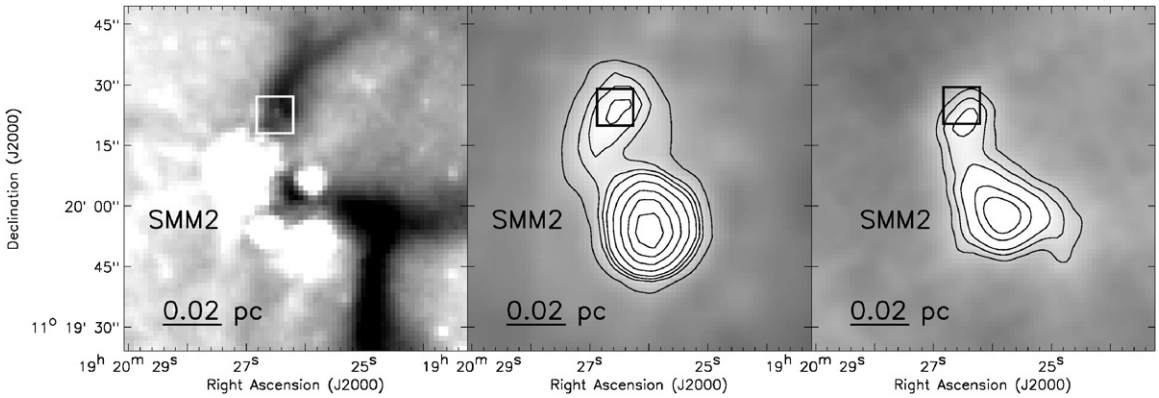

Figure 13. Left: *Spitzer* 8.0 μm image in gray scale indicating the location of the Class 0 candidate with respect to the submillimeter peak SMM2 (see Figures 8 and 9) and the dense filaments. The box denotes the Class 0 candidate's position. Middle: gray scale 70 μm image showing the envelope emission from the Class 0 candidate, with the 70 μm data as contours. Right: gray scale 350 μm image with the 350 μm contours overplotted. The Class 0 candidate is located at the center of both the 70 μm and 350 μm emission peaks. The contour levels in both cases were chosen arbitrarily to highlight the peaks centered at the Class 0 candidate.

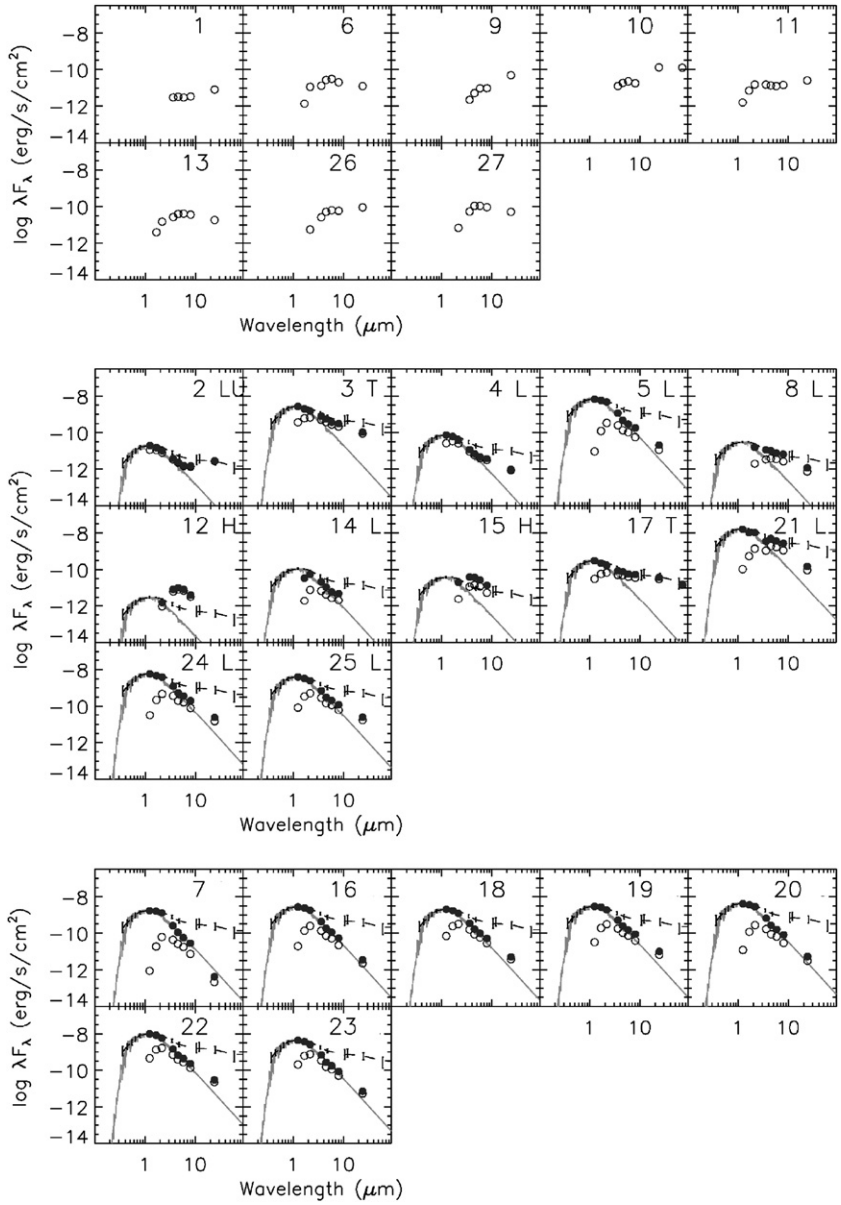

Figure 14. SEDs of the candidate YSO sample in L673. For the Class II and III YSOs the SEDs show the observed (open circles) as well as the dereddened fluxes (2MASS, IRAC, and MIPS; filled circles) for each source. The black-dashed line is the overplotted median SED for Classical T-Tauri stars (CTTs) of Taurus and the stellar model of a K7 star is also shown for comparison (black solid curve). Top: SEDs for Class I and Flat sources. Middle: SEDs for Class IIs. Bottom: SEDs for Class IIIs.

Table 6
Evolutionary Indicators of YSOs in L673

YSOs	L_{bol} ($M_\odot$)	T_{bol} (K)	L_{bol}/L_{smm}	Class Based on T_{bol}[a]	Spectral Slope α	Class Based on α
1	0.04	261	···	I	0.44	I
2	0.04	1291	···	II	−0.64	II
3	3.11	1246	···	II	−0.90	II
4	0.08	1746	···	II	−1.35	II
5	1.04	1264	···	II	−1.53	II
6	0.17	538	···	I	0.15	Flat
7	0.17	1303	···	II	−2.30	III
8	0.01	743	···	II	−0.49	II
9	2.06	32	79.5	0[b]	1.30	I
10	1.50	97	43.4	I[b]	0.98	I
11	0.24	377	···	I	0.18	Flat
12	0.02	851	···	II	−0.68	II
13	1.17	148	42.3	I[b]	0.16	Flat
14	0.02	1271	···	II	−0.76	II
15	0.03	868	···	II	−0.39	II
16	0.59	1341	···	II	−2.05	III
17	0.48	859	···	II	−0.35	II
18	0.88	1536	···	II	−1.93	III
19	0.89	1415	···	II	−1.67	III
20	0.74	1376	···	II	−1.96	III
21	7.69	987	···	II	−1.13	II
22	4.45	1592	···	II	−1.84	III
23	1.98	1613	···	II	−2.13	III
24	1.52	1289	···	II	−1.59	II
25	1.48	1438	···	II	−1.51	II
26	0.64	307	···	I	0.94	I
27	0.69	418	···	I	0.45	I
28[c]	0.43	33	···	0	0.74	I

Notes.
[a] T_{bol} does not differentiate between Class II and III objects.
[b] Also classified as Class 0 based on L_{bol}/L_{smm}.
[c] The Class 0 candidate from Section 4.3.

Table 7
Evolutionary Indicators of YSOs in CB188

YSOs	L_{bol} ($M_\odot$)	T_{bol} (K)	L_{bol}/L_{smm}	Class Based on T_{bol}	Spectral Slope α	Class Based on α
1	3.56	1543	···	II	−2.07	III
2	0.94	1368	···	II	−1.85	III
3	1.14	413	438.6	I	0.22	Flat

$$T_{bol} = 1.25 \times 10^{-11} \frac{\int_0^\infty \nu S_\nu d\nu}{\int_0^\infty S_\nu d\nu} K, \quad (3)$$

$$L_{smm} = 4\pi d^2 \int_0^{\nu=\frac{c}{350\,\mu m}} S_\nu d\nu, \quad (4)$$

where ν is the observed frequency, d is the distance of the source, c is the speed of light, and S_ν is the observed flux at frequency ν. The evolutionary indicators L_{bol} and T_{bol} were computed for all the YSOs while L_{bol}/L_{smm} was only computed for the sources with available data for $\lambda \geqslant 350\ \mu$m (Tables 6 and 7). As it can be seen in Figure 16, the T_{bol} classification limits are in very good agreement with the classification system based on the spectral slope of the SED. Four out of the five Class I and all four Flat sources fall in the Class I category with 70 K $\leqslant T_{bol} \leqslant$ 650 K (there are no separate limits for the Flat sources in the original classification by Chen et al. 1995). In addition, all of the Class II and III YSOs are within the bolometric temperature limits of Class II sources (the Class III YSOs cannot be distinguished from Class II objects using T_{bol}). Based on T_{bol} the outflow source (source ID 9) moves from a Class I to a Class 0 object, yielding a bolometric temperature of 32 K, while the new Class 0 candidate in L673 has a T_{bol} of 33 K and L_{bol} of 0.4 $L_\odot$ placing it among the few low-luminosity Class 0 candidates.

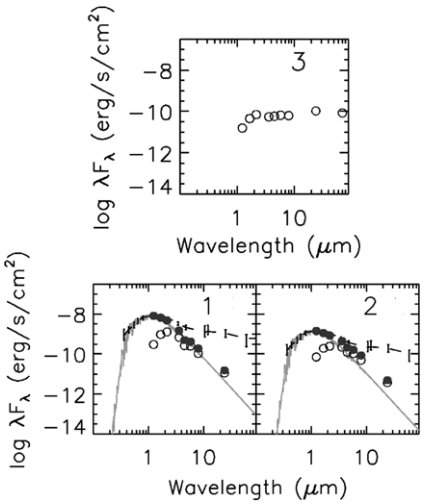

Figure 15. SEDs of the candidate YSO sample in CB188. Symbols and labels are similar to Figure 14.

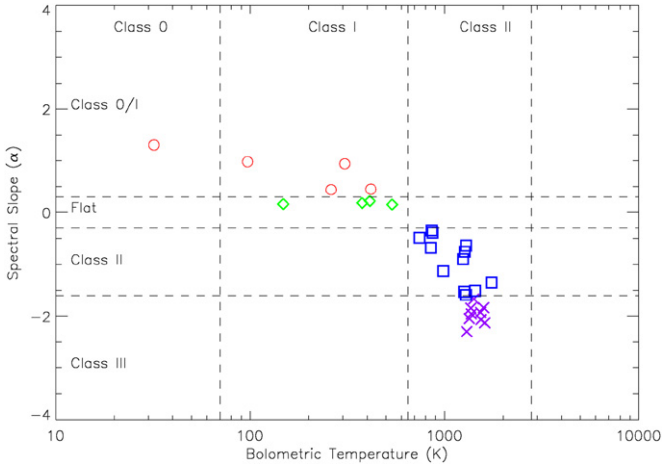

Figure 16. Spectral slope α of the SED plotted against the bolometric temperature T_{bol} for all the YSO candidates in L673 and CB188. The YSOs are color coded according to their spectral class: Class I protostars are plotted in red, Flat sources in green, Class II in blue, and Class III in purple. They also correspond to the symbols circle, diamond, square, and cross, respectively. It is apparent that the T_{bol} classification limits are in very good agreement with the classification system based on the spectral slope of the SED.
(A color version of this figure is available in the online journal.)

Evans et al. (2009) suggested bolometric temperature limits for Flat Spectrum Sources of 350 K < T_{bol} < 950 K. Using these limits for our sample in conjunction with the T_{bol} limits for the rest of the Classes we observe that out of the seven sources that lie within these limits, three are in fact "Flat" based on their spectral slope, three have Class II SEDs while the last one has a Class I SED. This range therefore includes 75% of the Flat Sources, 25% of the Class IIs and 25% of the Class Is as well. For comparison, Evans et al. (2009) computed percentages of 79%, 22% (also including Class IIIs) and 23%, respectively, using the same T_{bol} range for Flat sources on their sample. Our result is therefore consistent with Evans et al. (2009), although

with a very small sample of YSO candidates, so that a more conclusive statement cannot be drawn.

Only four of our YSOs have enough long-wavelength detections to determine the L_{bol}/L_{smm} ratio. Two of these have Class I SEDs (IDs : L673-9; outflow source, L673-10), and the other two are classified as Flat spectrum sources (source IDs: L673-13, CB188-3). All these sources apart from YSO 3 in CB188 have a ratio < 200 which places them in the Class 0 regime. For outflow source 9 this classification agrees with the T_{bol} value of <70 K. Tables 6 and 7 give a detailed list of these results including the classification of the YSOs based on these parameters.

4.7. Bolometric Luminosity–Temperature Diagram

The bolometric luminosity–temperature diagram (hereafter BLT diagram), L_{bol} versus T_{bol}, was first introduced by Myers & Ladd (1993) and Chen et al. (1995) as the H-R diagram for protostellar sources. There is ongoing evidence that the classic, single isothermal sphere (SIS) collapse model, which predicts a mass accretion rate that is constant in time (see review by Shu et al. 1987), is not in agreement with the low protostellar luminosities measured observationally, giving rise to the "Luminosity Problem" (Kenyon et al. 1990). In order to tackle this problem, Myers et al. (1998) proposed a YSO accretion rate that decreases exponentially with time due to envelope dissipation and modeled the infall termination as a gradual process rather than as a sudden stop of accretion. This approach resulted in model tracks on the BLT diagram which reflected an initial increase of the YSO's bolometric luminosity as it accumulates more and more mass from the envelope, and eventually trails off as envelope accretion significantly decreases, indicating a simultaneous decrease of the YSO's bolometric luminosity. On the other hand, Young & Evans (2005) used the BLT diagram to examine whether the YSO evolutionary tracks according to the classical inside-out collapse model (Shu 1977) would agree with the evolutionary "stages" of their sample using a classification based on both the SED spectral slope and the T_{bol} ranges. The Shu model assumes an initial envelope density that can be approximated by a singular isothermal sphere and scales as $\propto r^{-2}$, where r is the radius of the sphere. It predicts a dynamical, inside-out collapse of a sphere with an infinite central density and a constant envelope accretion rate throughout the protostar's evolution. Using these assumptions, the model predicts bolometric luminosities that increase in time until infall is terminated. The lower values of the predicted bolometric luminosities from the Myers model better agree with the observational data, although most of the observed luminosities are still too low to be explained by any of the model tracks. Evans et al. (2009) also show a BLT diagram for YSO sources in the large c2d clouds, many of which show the same underluminosity feature.

The BLT diagram of the total 31 YSO candidates, including the newly identified Class 0 protostar, is shown in Figure 17. The spread of L_{bol} & T_{bol} is similar to that found for the large c2d clouds by Evans et al. (2009), showing that L673 is similar to the c2d large clouds in this respect. Most of our observational data better agree with the model tracks that are characterized by exponentially decreasing accretion rates. However, many sources have bolometric luminosities too low to be explained by these models while very few of them lie very close to the model tracks described by Young & Evans (2005). The so-called "Luminosity Problem" has been encountered many times in the past and was first observed by

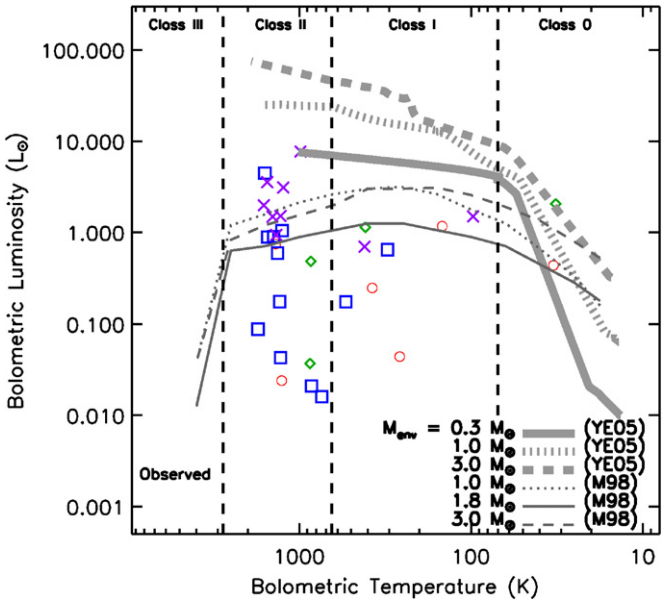

Figure 17. BLT diagram. The YSO colors and symbols; red (circle), green (diamond), blue (square), and purple (cross) correspond to SED classes. The thick lines in the diagram represent the evolutionary tracks according to the Shu (1977) model for a core with initial masses of 0.3, 1.0, and 3.0 $M_{\odot}$ (Young & Evans 2005) while the thin model tracks follow the assumptions of Myers et al. (1998) for initial masses of 1.0, 1.8, and 3.0 $M_{\odot}$.

(A color version of this figure is available in the online journal.)

Kenyon et al. (1990). Various theories have been proposed to account for the discrepancies between models and observations and give a plausible explanation for these very low observed luminosities. One of the most prevailing theories is non-steady accretion (Kenyon et al. 1990, 1994; Kenyon & Hartmann 1995), in which long quiescent accretion periods are followed by intense and irregular accretion rates whenever a large amount of accumulated mass is released onto the star (episodic accretion). Theoretical models from Vorobyov & Basu (2005, 2006) and Boss (2002) have found that such gravitational instabilities in the disk are a potential driver of the short-lived bursts toward the central protostar. This theory could justify the locations of most of the YSOs on the BLT diagram supporting the idea of very low accretion rates, and therefore low bolometric luminosities, followed by sudden FU-Orionis type variations. Dunham et al. (2010) present a set of evolutionary models that take into account the effects of opacity, mass-loss, outflow cavities, rotation and episodic accretion in order to provide a solution to the luminosity problem. They find results that strongly favor episodic accretion as the main process responsible for the low luminosities observed.

4.8. SED Modeling

For the modeling of the SEDs we used an online fitting tool (Robitaille et al. 2007). This tool uses a pre-computed grid of YSO models to fit the input SEDs. The grid encompasses a large range of stellar masses and YSO evolutionary stages and uses a total of 20,000 models or 200,000 SEDs taking into account various inclinations and apertures. As discussed in Robitaille et al. (2006), there are many advantages of fitting pre-computed SEDs to the data. Apart from the fact that it is very efficient when modeling large data sets, it allows us to make use of all available data without loss of information as well as infer the uniqueness or nonuniqueness of a fit from the range of model parameters that fit a certain SED.

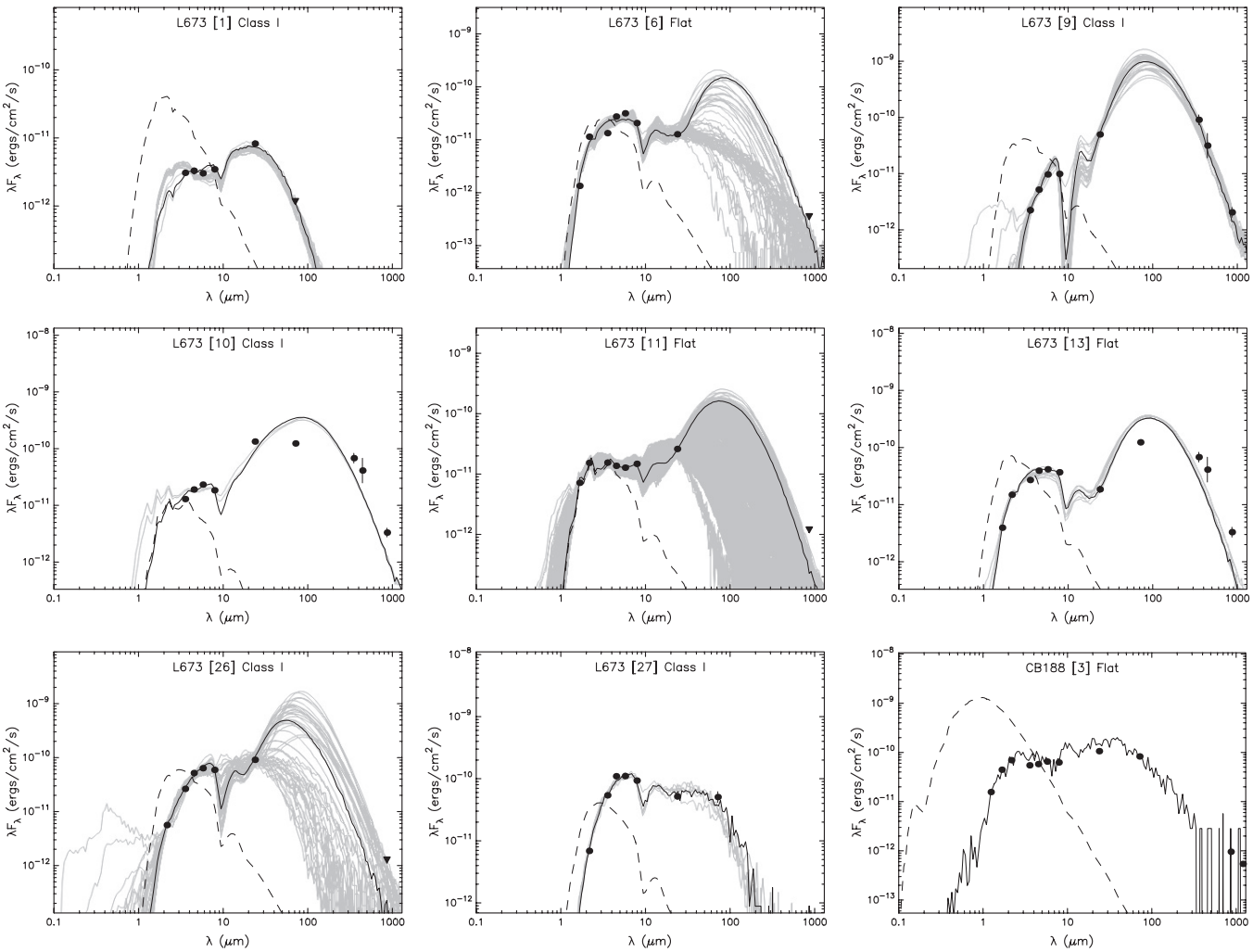

Figure 18. Class I and Flat SEDs. The black points are the observed data. The black solid line represents the model that gives the best fit to the input SED and the gray lines show the next best fit models for $\chi^2 - \chi^2_{\rm best} < 3 \times n_{\rm data}$. A model for the best stellar photosphere fit is overplotted in each case with black-dashed lines (it fits the interstellar extinction but does not include any envelope contribution).

We present the whole set of the SED models in Figures 18–21. The model SEDs in Figure 18 agree with the expected SED shapes of Class I and Flat Spectrum Sources. We obtained mean values for various model parameters such as disk and envelope masses as well as disk and envelope accretion rates by using the range of models given by the condition $\chi^2 - \chi^2_{\rm best} < 3 \times n_{\rm data}$ for each of the YSOs. Robitaille et al. (2007) explain that although this is an arbitrary cutoff, it provides a range of acceptable fits to the eye (see Robitaille et al. 2007 for more discussion on this cutoff condition). The mean values of the model parameters are given in Tables 8 and 9. However, we note that the ranges of values used to calculate the mean were rather large for some of the YSOs whose SEDs are not well-constrained.

The SED model of the Class 0 candidate agrees with the general form of Class I/0 SEDs, displaying a large amount of excess far-infrared emission relative to mid-infrared (Figure 19). This implies the presence of a surrounding envelope that contains large amounts of gas and dust and is currently accreting onto a disk. The modeling results yield a value for the envelope mass of 0.7 $M_\odot$ therefore supporting this idea and making the Class 0 nature of this source even more plausible.

Some of the modeling results for the YSOs' physical parameters will be discussed in the next section.

Table 8
L673 Model YSO Parameters for Class II YSOs

Source ID	YSO Class	$\chi^2_{\rm best}$	Disk Mass ($M_\odot$)	Disk Acc. Rate ($M_\odot$ yr^{-1})	Interstellar A_V (mag)
2	II	11.06	9.8×10^{-4}	5.9×10^{-10}	3.6
3	II	0.27	8.9×10^{-3}	3.2×10^{-8}	7.8
4	II	0.51	5.4×10^{-4}	3.3×10^{-10}	2.7
5	II	45.67[a]	2.3×10^{-7}	3.1×10^{-13}	23.0
8	II	1.28	1.2×10^{-3}	2.5×10^{-9}	28.0
12	II	195.87[b]	···	···	30
14	II	13.38[b]	···	···	26.3
15	II	146.54[b]	···	···	30
17	II	6.17	4.6×10^{-3}	2.1×10^{-8}	10.3
21	II	42.4	9.6×10^{-8}	2.7×10^{-12}	17.2
24	II	43.05[a]	2.5×10^{-7}	3.9×10^{-13}	19.4
25	II	13.96	5.7×10^{-4}	1.2×10^{-10}	14.1

Notes. The values listed below are the mean values obtained for $\chi^2 - \chi^2_{\rm best} < 3 \times n_{\rm data}$, where $n_{\rm data}$ is the number of data points.
[a] Possible borderline Class III objects with α of -1.53 and -1.59 for sources 5 and 24, respectively.
[b] SED of the source is fitted well by a stellar photosphere spectrum.

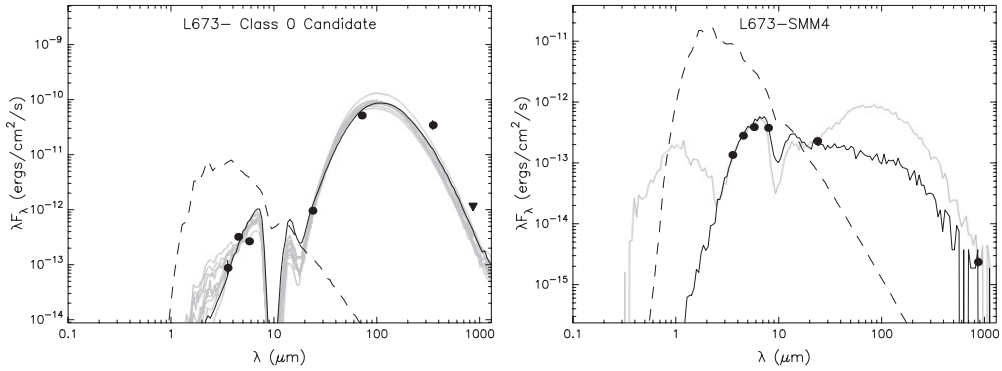

Figure 19. Left: model SED of the Class 0 candidate. Right: model SED of the possible YSO candidate in the submillimeter peak SMM4.

Table 9
L673 Model YSO Parameters for Class I and Flat Sources

L673 Source ID	YSO Class	$\chi^2_{\rm best}$	Disk Mass ($M_\odot$)	Envelope Mass ($M_\odot$)	Interstellar A_V (mag)
1	I	6.9	···	1.2×10^{-6}	28.8
6	Flat	45.6	8.8×10^{-3}	0.02	27.2
9	I	5.49	···	2.53	16.2
10	I	180.6	···	0.96	14.2
11	Flat	0.7	2.0×10^{-3}	0.03	20.6
13	Flat	154.24	1.6×10^{-3}	1.20	19.6
26	I	2.51	···	0.26	19.7
27	I	9.06	···	7.0×10^{-8}	25.4
28	0[a]	105.08	···	0.70	9.70
			CB188		
3	Flat	62.22	0.084	1.4×10^{-8}	3.5

Notes. The values listed below are the mean values obtained for $\chi^2 - \chi^2_{\rm best} < 3 \times n_{\rm data}$, where $n_{\rm data}$ is the number of data points.
[a] Class 0 candidate from Section 4.3.

4.9. YSO Accretion Rates

There have been many studies in the past regarding the disk accretion rates of YSOs especially for Classical T-Tauri Stars (CTTSs) as well as Intermediate Mass T-Tauri Stars (IMTTSs). Hartmann et al. (1998) measured the median accretion rate for a sample of TTSs in Taurus to be $10^{-8}\,M_\odot$ yr^{-1} while Valenti et al. (1993) and Gullbring et al. (1998) found the same value for separate samples of CTTSs in Taurus. Hartigan et al. (1991, 1995) obtained an accretion rate of $10^{-7}\,M_\odot$ yr^{-1} for CTTSs in Taurus and a median of $4 \times 10^{-9}\,M_\odot$ yr^{-1} for sources in Chamealeon I. Calvet et al. (2004) obtained an average accretion rate for nine IMTTSs of $3 \times 10^{-8}\,M_\odot$ yr^{-1} while median accretion rates of the order of $10^{-8}\,M_\odot$ yr^{-1} were also found for Class II sources in ρ Ophiuchus by Muzerolle et al. (1998a, 1998b). The mean mass infall rate for Class I sources in Taurus was studied by Kenyon et al. (1993a, 1993b) and they obtained results consistent with the predictions of the Shu (1977) inside-out collapse model, $4 \times 10^{-6}\,M_\odot$ yr^{-1}. Finally, an infall rate as high as $10^{-4}\,M_\odot$ yr^{-1} has been predicted for canonical FU Ori objects (Bell & Lin 1994; review by Hartmann & Kenyon 1996).

4.9.1. Model Disk Accretion Rates & Disk Masses

For comparison, the disk accretion rate range for Class II objects obtained through modeling the SEDs of our YSO sample and excluding high and low end values is 4×10^{-13} to $3 \times 10^{-8}\,M_\odot$ yr^{-1} (Table 8). However, two of the Class II YSOs that lie at the low end of the disk accretion rate are very

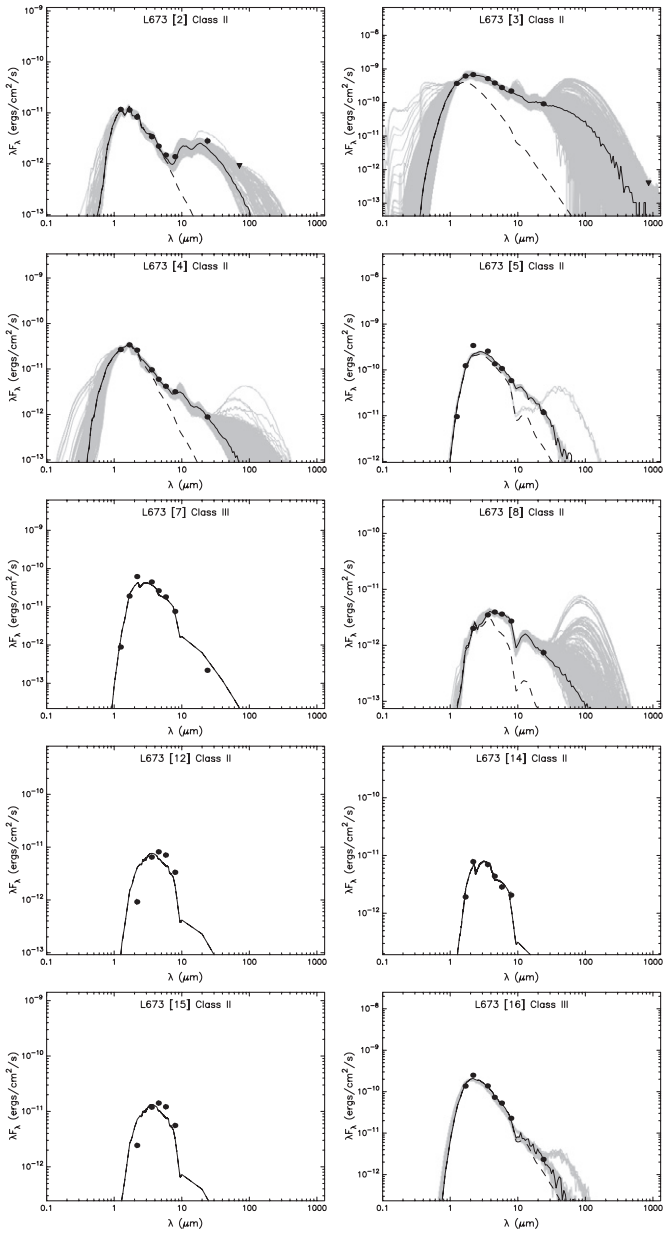

Figure 20. Model SEDs of the Class II and III YSO candidates. YSOs 7, 12, 14, and 15 are fitted well by a stellar photosphere spectrum.

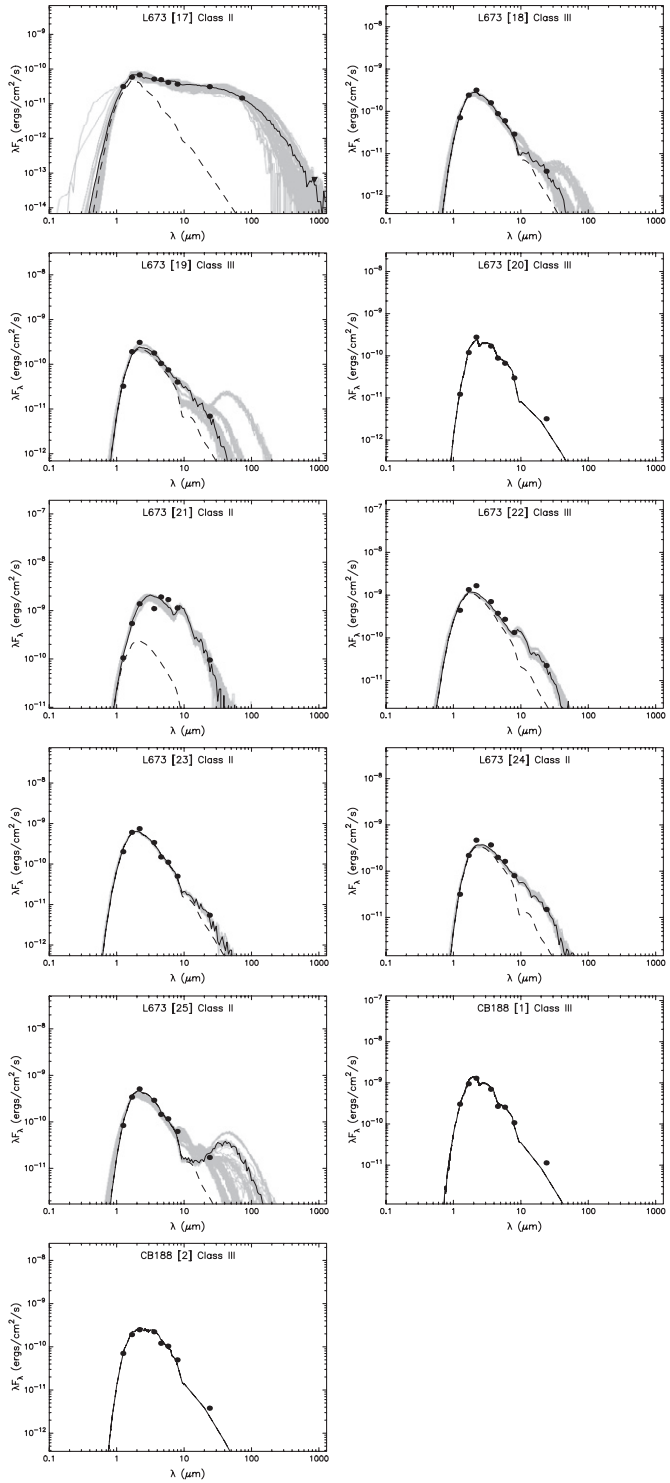

Figure 21. Model SEDs of the Class II and III YSO candidates. YSOs L673-20, CB188-1 and 2 are fitted well by a stellar photosphere spectrum.

likely to be borderline Class III objects, with α of -1.53 and -1.59, and model disk masses of the order of $10^{-7}\,M_{\odot}$. Taking this into consideration, we constrain our disk accretion rate range for Class II objects to 3.3×10^{-10} to $3 \times 10^{-8}\,M_{\odot}$ yr^{-1} with peak disk masses from 10^{-4} to $10^{-3}\,M_{\odot}$. For disks around Class II objects, 2MASS, IRAC, and MIPS1 data are sufficient for determining the disk masses although this is not the case for embedded sources due to envelope confusion. The minimum values of the disk accretion rate ranges are lower than others previously found. This may be the case as it is not possible to calculate the accretion rates for all observed T-Tauri stars and also because earlier studies may have been restricted to the more luminous stars due to observational sensitivity. On the other hand, the values at the low end of the Class II disk accretion rates might suggest that there has been a misclassification of some of the YSOs, and therefore a more well-sampled SED would significantly improve these results (e.g., by using future Herschel observations).

4.9.2. Model Envelope Masses

The peak envelope masses we obtain for Class I/0 and Flat sources range from 0.01 to 1.0 $M_{\odot}$ (Table 9). We do not calculate any mean or median values because of the small size of our sample. The envelope accretion rates could not be well constrained due to the lack of well-sampled SEDs, and are therefore not presented. However, the envelope masses are well constrained by the shape of the long wavelength SED.

Enoch et al. (2009) calculated the envelope masses of a large sample of Class 0 and I protostars in Perseus, Serpens, and Ophiuchus. Omitting high and low end values, they find masses in the range of 0.11 to 3.66 $M_{\odot}$ for 64 protostars in Perseus, 0.17 to 3.72 $M_{\odot}$ for 32 protostars in Serpens, and 0.03 to 0.53 $M_{\odot}$ for 26 protostars in Ophiuchus. The corresponding mean values are 1.027, 1.2, and 0.14 $M_{\odot}$, which agree with our range of model values.

Three of the model envelope masses we found are significantly lower than the values of the rest of our sample, and also significantly lower than those found by Enoch et al. (2009) for Class I and Flat sources. YSOs L673-1, L673-27, and CB188-3 have envelope masses of the order of 10^{-6} and 10^{-8} (Table 9). L673-1 and L673-27 lack submillimeter data to constrain their envelope, and the 70 μm flux is an upper limit in the case of L673-1. We therefore believe that the models gave such inconsistent results for the envelope mass of these two sources because of the lack of millimeter and submillimeter SED points. Kauffmann et al. (2008) obtained a mass of 0.3 $M_{\odot}$ for CB188-3 while Chen et al. (2007) a mass of 0.7 $M_{\odot}$. Since the bolometric luminosity and temperature that we measure for the same protostar agree with the results from Kauffmann et al. (2008), we believe that the large deviation of the envelope masses arises due to the poor fit from the best χ^2 model. Looking back at Figure 18 and comparing the SED model of CB188-3 to the model of L673-26, we observe the following; both models show submillimeter flux values of the same order of magnitude and similar infrared fluxes that are slightly more flattened for CB188-3. However, the mean envelope mass that we obtain for L673-26 is $\sim$0.26 $M_{\odot}$. Taking into consideration that the range of models given by $\chi^2 - \chi^2_{\rm best} < 3 \times n_{\rm data}$ give us only one model SED for CB188-3, we believe that the result of this fit is not representative of the actual envelope mass of this source. Therefore, this possibly hints that modeling all three sources individually, when additional SED points are incorporated from future observations, rather than fitting pre-computed models to the SEDs would be required to obtain more accurate values.

4.10. L673 & CB188 in Comparison to Other c2d Clouds

Studying isolated star formation is essential for understanding the physical processes that take place as a single core gradually transforms into one or multiple star-forming regions. Studies in large cloud complexes are hindered by interactions with neighboring cores of different evolutionary stages and star

formation activity that significantly affect and alter a core's physical evolution. A simple picture of star formation can therefore be obtained through studying isolated cores, like the ones observed as part of the c2d observations.

L673 and CB188 are very different when it comes to their star formation activity and core structure. L673 has a very filamentary structure with multiple sites of star formation while CB188 is a small and quiescent globule-like core that harbors a very small YSO population. The star formation efficiency (SFE) of L673, was measured using a mass estimate of 290($\pm$30%) $M_\odot$ derived from an extinction map (T. Huard, private communication). The extinction map that was used for the derivation of the cloud mass was created using 2MASS and c2d data, by means of the Weingartner & Draine (2001) extinction law to determine A_V (Evans et al. 2009). The total mass was then computed assuming $N(\mathrm{H_2}) = 1.37 \times 10^{21} A_V$ cm^{-2} mag^{-1}, which is an updated version (see Draine 2003; Evans et al. 2009) of the relation first published by Bohlin et al. (1978). It uses the relation $N_\mathrm{H}/A_V = (1.086 C_\mathrm{ext}(\mathrm{V}))^{-1}$ from Draine (2003), with C_ext(V) taken from the online tables[5] for $R_V = 5.5$. For the derivation of the SFE we use the relation by Evans et al. (2009), assuming a mean stellar mass of 0.5 $M_\odot$, and a total YSO population of 28 YSO candidates in L673. We do not compute an SFE for CB188 as its YSO population is too small to obtain a meaningful result:

$$\mathrm{SFE} = \frac{M_\mathrm{yso}}{M_\mathrm{yso} + M_\mathrm{cloud}}. \quad (5)$$

We compute an SFE of 4.6% which agrees with the 3%–6% SFE range that Evans et al. (2009) computed for the whole c2d sample and is therefore very similar to the SFEs of the larger c2d clouds. In comparison, Visser et al. (2002) derived a mass of 87.4 $M_\odot$ for L673 from their 850 μm data focusing on a much smaller area that encloses the main star-forming regions of L673. As submillimeter data traces only higher column densities, the significantly higher SFE of $\sim$14% that we obtain using this estimate reflects the SFE of the dense regions in L673, while the previous result is representative of the cloud's SFE as a whole.

Similar c2d studies of the YSO population of nearby isolated clouds have not revealed more than 26 YSOs in most cases. Small clouds such as L1251B and B59 have revealed 18 (Lee et al. 2006) and $\sim$20 (Brooke et al. 2007) YSOs respectively while Alcalá et al. (2008) presented 26 YSO candidates for the larger Chamaeleon II cloud. Kirk et al. (2009) identified 39 YSO candidates in L1251A, L1251B and L1251W combined, with the majority being in the L1251A core. Very Low Luminosity Objects (VeLLOs) have been discovered in some of the isolated, dense cores such as in L328 (Lee et al. 2009), IRAM 04191+1522 (Dunham et al. 2006) and L1521F (Bourke et al. 2006), with luminosities $< 0.1\ L_\odot$. The YSO population of L673 is fairly large for a small, isolated cloud: 27 YSO candidates are detected using the c2d photometric criteria (Section 3.1 & 4.1), therefore resembling L1251B and B59, and 3 YSO candidates in CB188 bringing the total number to 30 YSO candidates.

We briefly discuss here the *IRAS* sources that were previously detected in L673 and CB188 in order to confirm or reject the YSO nature of these *IRAS* sources based on the c2d data, and to emphasize the much larger YSO sample we obtained using the more sensitive c2d observations. Parker (1988) created an *IRAS* point source catalog associated with opacity class 6 clouds from the Lynds Catalog of Dark Nebulae, and discussed their distribution and properties. The properties of some *IRAS* sources with good quality detections were further discussed in Parker 1991. Only nine *IRAS* sources were previously known in L673, eight of which are presented in Parker 1988, and five of them seem to be associated with embedded sources. We select as YSO candidates the *IRAS* sources whose fluxes increase in at least two bands with the flux at the longer wavelength band being a detection and not an upper limit (Evans et al. 2003). The complete list of the *IRAS* sources is given in Tables 10 and 11, along with their coordinates, fluxes (from Visser et al. 2002), YSO association, and their classification by c2d. Five *IRAS* sources feature rising fluxes in two consecutive bands, and two of them are associated with YSO candidates, IRAS 19180+1114 and IRAS 19181+1112. The latter coincides with a Class II YSO while the former seems to be associated with three of the YSOs in SMM2 (Class I, Flat and Class II). IRAS 19181+1056, 19184+1055, and 19180+1116 also feature rising fluxes but are nevertheless classified by c2d as "star," "rising" or "one" (see Table 10). The rest of the *IRAS* sources do not satisfy the requirements of increasing fluxes in two bands. However, IRAS 19184+1118 does correspond to a Class II YSO candidate by c2d.

CB188 is known to have two *IRAS* sources, 19179+1129 and 19180+1127. IRAS 19179+1129 is associated with the Flat Spectrum Source that was identified by the c2d photometric criteria, while IRAS 19180+1127 is out of the IRAC field of view (Table 11).

4.11. Filamentary Structure, Class I Clustering, and Thermal Fragmentation

As one can see from the optical images, L673 has a very filamentary structure with strikingly dense concentrations that can also be seen in the IRAC 8 μm image. The 850 μm dust emission corresponds very well to the optical extinction (there are a couple of exceptions where 850 μm emission is not related with any dense structures but this is due to data taking artifacts at 850 μm and those regions are not considered in the analysis).

The groups of Class I & Flat YSOs that are of particular interest to us, namely SMM1 and SMM2, are also located in the visually extincted areas. It was mentioned earlier that the YSOs associated with those two peaks are tightly clustered and in the case of SMM1 the two Class I and two Flat sources lie in a straight line in projection, with this line being perpendicular to the larger scale elongation of the filament (see Figures 8–10). We were therefore intrigued to examine whether the YSO separations in these two regions are consistent with the theory of thermal fragmentation by computing the cloud's Jeans Length. The Jeans Length determines the critical radius of a cloud at which gravity prevails against external pressure causing the gravitational collapse of the cloud and is given by

$$\lambda_J = \sqrt{\frac{\pi k_B T}{G m \rho}} = 0.2\ \mathrm{pc} \left(\frac{T}{10\ \mathrm{K}}\right)^{1/2} \left(\frac{n}{10^4\ \mathrm{cm^{-3}}}\right)^{-1/2}, \quad (6)$$

where ρ is the mean mass density of the cloud, n is the mean particle density, m is the mean molecular mass, T is the

[5] http://www.astro.princeton.edu/~draine/dust/dust.html

Table 10
IRAS Sources[a] in L673 and c2d Classification

Source	R.A. (J2000)	Decl. (J2000)	Fν(12 μm)[b] (Jy)	Fν(25 μm)[b] (Jy)	Fν(60 μm)[b] (Jy)	Fν(100 μm)[b] (Jy)	YSO[c] Association /YSO Source ID	Rising Flux[d]	c2d Classification
19180+1116	19 20 22.5	+11 22 07.0	1.09	2.22	3.51L	87.21L	No	Yes	One[e] or Star[f]
19180+1114	19 20 25.8	+11 19 52.0	0.41L	1.60	2.55L	105.70L	Yes/10, 13, 14	Yes	3 YSOs: Class I, II & Flat
19181+1056	19 20 30.9	+11 01 54.8	1.71	2.81	3.69	87.16L	No	Yes	Star
19181+1112	19 20 30.7	+11 17 56.0	0.38L	0.43	5.59L	106.70L	Yes /17	Yes	Class II
19181+1059	19 20 32.5	+11 05 39.0	3.74	3.55	5.18L	91.15L	No	No	Star or Rising[g]
19183+1123[h]	19 20 44.0	+11 28 55.0	0.96	0.50	5.53L	82.50L	No	No	Star
19184+1055	19 20 45.8	+11 00 57.8	3.74	5.46	3.69L	9.69	No	Yes	Rising
19184+1118	19 20 45.6	+11 23 50.0	2.95	1.07	5.45L	71.62L	Yes /21	No	Class II
19190+1105	19 21 26.9	+11 10 57.0	1.32	1.01	24.52L	86.05L	No	No	Star

Notes.
[a] From Parker (1988).
[b] Fluxes from Visser et al. (2002). Letter "L" denotes an upper limit.
[c] YSO candidates selected by the c2d photometric criteria.
[d] Rising flux in two consecutive bands, with the flux of the longer wavelength band being a detection and not an upper limit. Fluxes from Visser et al. (2002).
[e] Detected in only one band between IRAC1–IRAC3.
[f] Sources classified as stars by c2d have fluxes that can be fitted well by a reddened stellar photosphere in at least three bands.
[g] Classified according to SED morphology: source features a rising SED.
[h] Not associated with dark cloud by Parker (1988).

Table 11
IRAS Sources in CB188 and c2d Classification

Source	R.A. (J2000)	Decl. (J2000)	YSO[a] Association /YSO Source ID	c2d Classification
19179+1129	19 20 14.9	11 35 35	Yes/3	Flat source
19180+1127	19 20 21.0	11 32 54	No	... [b]

Notes.
[a] YSO candidates selected by the c2d photometric criteria.
[b] Source is out of the IRAC field of view.

temperature of the cloud, G is the gravitational constant, and k_B is Boltzmann's constant. Anglada et al. (1997) determined an upper limit for the rotational temperature of L673 of $T_{\rm rot} \leqslant 12$ K by making use of NH_3 observations, implying that the kinetic temperature is $\leqslant$13 K (Tafalla et al. 2004). We use a value of 12 K for our calculations. We attempt to determine the mean density using two different methods, one involving A_V measurements of the region and one that is based on the 850 μm submillimeter dust continuum emission map.

4.11.1. Mean Density Derived from Interstellar Extinction

We use the following empirical formula from Evans et al. (2009) that directly relates the column density with the interstellar extinction A_V. This relation was discussed in Section 4.10:

$$N(\mathrm{H_2}) = 1.37 \times 10^{21} A_V \ \mathrm{cm^{-2}\ mag^{-1}}. \quad (7)$$

We subtract an average background interstellar extinction of ~5 mag, measured from our A_V map, from the peak value, ~19 mag, and therefore adopt a peak extinction, of 14 magnitudes that we use to measure the column density. Using this value we obtain a mean column density for SMM1 & SMM2 of 1.9×10^{22} cm^{-2}. We measure the size of the region using an A_V contour of 14 magnitudes, as the extinction starts to rapidly increase compared to the background surrounding cloud at this value. Since the width of the core using this particular A_V is similar for both SMM1 and SMM2, we adopt an approximate value for the width for both of ~100″ or $\sim 4.5 \times 10^{17}$ cm. Assuming that the width of the cloud corresponds to its line-of-sight depth, we compute a mean density of $n(\mathrm{H_2}) \sim 4.2 \times 10^4$ cm^{-3}.

4.11.2. Mean Density Derived from 850 μm Observations

We can compare this result with the mean density computed from the 850 μm flux for these regions. We can calculate the column densities directly using the following relation from Visser et al. (2002) that assumes a temperature of 12 K, molecular weight ~ 1.36, beam solid angle 15″, and dust opacity at 850 μm of 0.012 cm^2 g^{-1}:

$$N(\mathrm{H_2}) = 1.33 \times 10^{20} \frac{F_{850_{\mu\mathrm{m}}}}{\mathrm{mJy(beam^{-1})}} \ \mathrm{cm^{-2}}. \quad (8)$$

Using the mean flux for SMM1 in a 50″ aperture we find a column density of 3×10^{22} cm^{-2} while the column density for SMM2 becomes 3.8×10^{22} cm^{-2} for an 850 μm flux computed within a 70″ aperture. These aperture sizes were used so that they included most of the bright, dust emission of the two peaks. For comparison, Visser et al. (2002) calculated a mean column density of 4×10^{21} cm^{-2} using 850 μm data which is lower than our column density estimate by a factor of 10. This is due to the fact that Visser et al. (2002) used the full maps of the 850 μm emission for the calculation while on the other hand we computed the column densities using aperture sizes centered only on the high density regions. We select the half-power contours of the 850 μm peaks to approximately define the size of the core. For SMM1, we measure the width of the core to be ~30″, or $\sim 1.4 \times 10^{17}$ cm, and for SMM2 we obtain a width of ~42″, or $\sim 1.9 \times 10^{17}$ cm. The resulting mean densities are 2×10^5 cm^{-3} and 3.8×10^5 cm^{-3} for SMM1 and SMM2, respectively, which are larger than the mean densities derived from the interstellar extinction by approximately a factor of 10. This is due to the fact that the 850 μm emission traces regions of

higher column density and that the core sizes we obtain are much smaller than the ones derived from the interstellar extinction.

4.11.3. Jeans Length

The Jeans lengths we compute using the densities derived from the 850 μm mean fluxes are ∼0.051 pc for SMM1 and ∼0.037 pc for SMM2. The mean angular near-neighbor separation of the four YSOs in SMM1 is ≈ 9″ or 0.013 pc while we previously measured the size of the core to be at least 30″, or 0.043 pc. Similarly, the mean angular near-neighbor separation of the YSOs in SMM2 is ≈10″, or 0.014 pc, while the overall angular size of the region is at least 42″, so 0.061 pc. We can see that the Jeans length in the case of SMM1 is greater than the YSO's separation by approximately a factor of ∼4, and by a factor of ∼3 in SMM2. It can further be seen that the Jeans lengths are similar to the core sizes measured from the 850 μm data. This could suggest that each core should have formed a single star if thermal fragmentation was the only important process at work. In comparison, the mean density derived from the interstellar extinction gives a Jeans length of ∼0.112 pc for both regions, which is larger than the near-neighbor separations of the YSOs by a factor of ∼10 for both SMM1 and SMM2, and about twice as large as the cores.

The values we obtain for the Jeans length are very likely to be underestimated as our input density reflects the current density of the cores rather than the initial density, when the core first became gravitationally unstable, which would probably have been much lower. We therefore think of the Jeans length estimates as lower limits, and expect the initial, true values to be much larger. To obtain a rough idea of what the current densities would have to be in order for the Jeans length to equal the near-neighbor separations we observe, we use Equation (6) and obtain a mean density $n_{\rm SMM1} \sim 3.2 \times 10^6$ cm^{-3} for SMM1, and $n_{\rm SMM2} \sim 2.7 \times 10^6$ cm^{-3} for SMM2. Both values are greater than the true current values by about a factor of ∼10.

Since the Jeans length greatly exceeds the near-neighbor separations of the associated regions (SMM1 & SMM2), thermal fragmentation cannot be the only physical process responsible for the formation of such dense YSO groups. Consequently, turbulence and shock waves may have had a significant effect on the gas and dust condensations resulting in the cloud's filamentary structure. In the case of SMM2, the YSOs have formed at the part of the filament where there is a clear bend (see Figure 13). Tobin et al. (2010) suggest that gravitational focusing could be the physical process responsible for the formation of protostars near such turns in the filaments (theoretical work by Burkert & Hartmann 2004), a theory which is consistent with the turbulent fragmentation of clouds. In this scenario, gravity focal points are created when the faster moving ends of a filament encounter a slowly moving medium and result in material flowing toward the focal point from orthogonal directions.

5. SUMMARY AND CONCLUSIONS

We have used the *Spitzer* c2d observations for the isolated star-forming cores L673 and CB188 to identify, characterize, and model all of the YSOs included in these regions. The main results presented in this paper are summarized below.

1. We identified 28 YSOs in L673 and an additional 3 in CB188. The population of 31 YSOs in both cores corresponds to Class percentages of ∼19%, 13%, and 39% for Class I, Flats, and Classes II & III, respectively, similar to that found for the large c2d clouds by Evans et al. (2009).
2. Most of the Class I & Flat Sources are closely spaced in regions of high A_V, which is indicative of the core's primordial structure while Classes IIs and IIIs are more evenly dispersed.
3. We identify a new Class 0 candidate in L673. We find that it occupies bright peaks at 70 and 350 μm and obtain a model SED whose shape is that expected for Class 0/I sources. The evolutionary indicator $T_{\rm bol}$ also places it in the Class 0 range with a value of ∼33 K, and with $L_{\rm bol} \sim 0.4\ L_\odot$.
4. The values of the evolutionary indicators $T_{\rm bol}$, $L_{\rm bol}/L_{\rm smm}$ as well as $L_{\rm bol}$ were computed for the YSO population where possible. We find that the $T_{\rm bol}$ classification limits are in very good agreement with the classification system based on the spectral slope of the SED. When incorporating the $T_{\rm bol}$ limits for Flat spectrum sources suggested by Evans et al. (2009) we see that the majority of Flat Sources (defined by α), ∼75%, are also included in this temperature range.
5. The model tracks on the BLT diagram for the 31 YSOs are inconsistent with the very low luminosities of the YSOs, implying lower values for the current accretion rates and therefore supporting the "episodic accretion" theory for the luminosity problem.
6. From the SED modeling we find that the disk masses for most Class II YSOs peak at 10^{-4} to $10^{-3}\ M_\odot$ while their disk accretion rates lie in the range of 3.3×10^{-10} to $3 \times 10^{-8}\ M_\odot$ yr^{-1}, consistent with more detailed studies of T Tauri stars. On the other hand, Class I and Flat sources have model envelope masses showing a distribution of 0.01 to $1.0\ M_\odot$, similar to the values observed around other Class I protostars.
7. The SFE we compute for L673 using a mass estimate of 290% ± 30% $M_\odot$ is 4.6%, a result which is in agreement with the SFE range of 3–6% measured for the five large c2d clouds (Evans et al. 2009). The mass estimate of $87\ M_\odot$, which was derived from 850 μm observations (Visser et al. 2002), gives us an SFE of ∼14% for the dense regions of L673.
8. We measure mean densities in the submillimeter peaks SMM1 and SMM2, where there is significant clustering of Class I & Flat sources, of 2×10^5 cm^{-3} and 3.8×10^5 cm^{-3} using 850 μm observations. The corresponding Jeans length we compute for these regions is 0.051 and 0.037 pc respectively, with near-neighbor YSO separations of 0.013 and 0.014 pc. An approximate mean density of $\sim 4.2 \times 10^4$ cm^{-3} was derived from the peak interstellar extinction of SMM1 and SMM2 with a resulting Jeans length ∼0.112 pc.
9. The Jeans length of the regions SMM1 & SMM2 measured from 850 μm data is higher than the near-neighbor YSO separations of the YSOs by a factor of ∼3 to 4 and also by a factor of ∼10 when using the mean density estimated from the interstellar extinction. Hence, we suggest that thermal fragmentation is not the dominant process of star formation in these regions.

A.E.T. thanks the University of Southampton for sponsoring the visiting student program at the CfA. Partial support for A.E.T and T.L.B. was provided by NASA through contracts 1279198, 1288806, and 1365763 issued by the Jet Propulsion Laboratory, California Institute of Technology, to the Smithsonian Astronomical Observatory.

REFERENCES

Alcalá, J. M., et al. 2008, ApJ, 676, 427
Allen, L. E., et al. 2004, ApJS, 154, 363
André, P., Ward-Thompson, D., & Barsony, M. 1993, ApJ, 406, 122
Anglada, G., Sepulveda, I., & Gomez, J. F. 1997, A&As, 121, 255
Armstrong, J. T., & Winnewisser, G. 1989, A&A, 210, 373
Bell, K. R., & Lin, D. N. C. 1994, ApJ, 427, 987
Bohlin, R. C., Savage, B. D., & Drake, J. F. 1978, ApJ, 224, 132
Boss, A. P. 2002, ApJ, 576, 462
Bourke, T. L., et al. 2006, ApJ, 649, L37
Brooke, T. Y., et al. 2007, ApJ, 655, 364
Burkert, A., & Hartmann, L. 2004, ApJ, 616, 288
Calvet, N., Muzerolle, J., Briceño, C., Hernández, J., Hartmann, L., Saucedo, J. L., & Gordon, K. D. 2004, AJ, 128, 1294
Calvet, N., et al. 2005, ApJ, 630, L185
Chen, H., Myers, P. C., Ladd, E. F., & Wood, D. O. S. 1995, ApJ, 445, 377
Chen, X., Launhardt, R., & Henning, T. 2007, ApJ, 669, 1058
Crapsi, A., van Dishoeck, E. F., Hogerheijde, M. R., Pontoppidan, K. M., & Dullemond, C. P. 2008, A&A, 486, 245
Currie, T., et al. 2009, ApJ, 698, 1
D'Alessio, P., Calvet, N., Hartmann, L., Lizano, S., & Cantó, J. 1999, ApJ, 527, 893
Di Francesco, J., Johnstone, D., Kirk, H., MacKenzie, T., & Ledwosinska, E. 2008, ApJS, 175, 277
Draine, B. T. 2003, ARA&A, 41, 241
Dunham, M. M., Crapsi, A., Evans, N. J., Bourke, T. L., Huard, T. L., Myers, P. C., & Kauffmann, J. 2008, ApJ, 179, 249
Dunham, M. M., Evans, N. J., Terebey, S., Dullemond, C. P., & Young, C. H. 2010, ApJ, 710, 470
Dunham, M. M., et al. 2006, ApJ, 651, 945
Enoch, M. L., Corder, S., Dunham, M. M., & Duchene, G. 2009, ApJ, 707, 103
Evans, N. J., et al. 2003, PASP, 115, 965
Evans, N. J., et al. 2007, Final Delivery of Data from the c2d Legacy Project: IRAC and MIPS (Pasadena: SSC)
Evans, N. J., et al. 2009, ApJ, 181, 321
Fazio, G. G., et al. 2004, ApJS, 154, 10
Feigelson, E. D., & Montmerle, T. 1999, ARA&A, 37, 363
Greene, T., & Lada, C. 1996, AJ, 112, 2184
Greene, T. P., Wilking, B. A., Andre, P., Young, E. T., & Lada, C. J. 1994, ApJ, 434, 614
Gullbring, E., Hartmann, L., Briceño, C., & Calvet, N. 1998, ApJ, 492, 323
Gutermuth, R. A., Megeath, S. T., Myers, P. C., Allen, L. E., Pipher, J. L., & Fazio, G. 2009, ApJS, 184, 18
Hartigan, P., Edwards, S., & Ghandour, L. 1995, ApJ, 452, 736
Hartigan, P., Kenyon, S. J., Hartmann, L., Strom, S. E., Edwards, S., Welty, A. D., & Stauffer, J. 1991, ApJ, 382, 617
Hartmann, L., Calvet, N., Gullbring, E., & D'Alessio, P. 1998, ApJ, 495, 385
Hartmann, L., & Kenyon, S. J. 1996, ARA&A, 34, 207
Harvey, P., Merín, B., Huard, T. L., Rebull, L. M., Chapman, N., Evans, N. J., II., & Myers, P. C. 2007, ApJ, 663, 1149
Harvey, P. M., et al. 2006, ApJ, 644, 307
Herbig, G. H., & Jones, B. F. 1983, AJ, 88, 1040
Hernández, J., et al. 2007, ApJ, 671, 1784
Jørgensen, J. K., et al. 2006, ApJ, 645, 1246
Kandori, R., et al. 2005, AJ, 130, 2166
Kauffmann, J., Bertoldi, F., Bourke, T. L., Evans, N. J., II, & Lee, C. W. 2008, A&A, 487, 993
Kenyon, S. J., Calvet, N., & Hartmann, L. 1993a, ApJ, 414, 676
Kenyon, S. J., Gomez, M., Marzke, R. O., & Hartmann, L. 1994, AJ, 108, 251
Kenyon, S. J., & Hartmann, L. 1995, ApJS, 101, 117
Kenyon, S. J., Hartmann, L. W., Strom, K. M., & Strom, S. E. 1990, AJ, 99, 869
Kenyon, S. J., Whitney, B. A., Gomez, M., & Hartmann, L. 1993b, ApJ, 414, 773
Kirk, J. M., et al. 2009, ApJS, 185, 198
Lada, C. J. 1987, IAU Circ., 115, 1
Lada, C. J., et al. 2006, AJ, 131, 1574
Lee, C. W., et al. 2009, ApJ, 693, 1290
Lee, J., et al. 2006, ApJ, 648, 491
Lonsdale, C. J., et al. 2003, PASP, 115, 897
Merín, B., et al. 2008, ApJS, 177, 551
Morata, O., Estalella, R., Lopez, R., & Planesas, P. 1997, MNRAS, 292, 120
Morata, O., Girart, J. M., & Estalella, R. 2003, A&A, 397, 181
Morata, O., Girart, J. M., & Estalella, R. 2005, A&A, 435, 113
Muzerolle, J., Allen, L., Megeath, S., Hernández, J., & Gutermuth, R. 2010, ApJ, 708, 1107
Muzerolle, J., Hartmann, L., & Calvet, N. 1998a, AJ, 116, 455
Muzerolle, J., Hartmann, L., & Calvet, N. 1998b, AJ, 116, 2965
Myers, P. C., Adams, F. C., Chen, H., & Schaff, E. 1998, ApJ, 492, 703
Myers, P. C., Fuller, G. A., Mathieu, R. D., Beichman, C. A., Benson, P. J., Schild, R. E., & Emerson, J. P. 1987, ApJ, 319, 340
Myers, P. C., & Ladd, E. F. 1993, ApJ, 413, L47
Noriega-Crespo, A., et al. 2004, ApJS, 154, 352
Parker, N. D. 1988, MNRAS, 235, 139
Parker, N. D. 1991, MNRAS, 251, 63
Rieke, G. H., et al. 2004, Proc. SPIE, 548, 50
Robitaille, T. P., Whitney, B. A., Indebetouw, R., & Wood, K. 2007, ApJ, 169, 328
Robitaille, T. P., Whitney, B. A., Indebetouw, R., Wood, K., & Denzmore, P. 2006, ApJ, 167, 256
Schechter, P. L., Mateo, M., & Saha, A. 1993, PASP, 105, 1342
Shu, F. H. 1977, ApJ, 214, 488
Shu, F. H., Adams, F. C., & Lizano, S. 1987, ARA&A, 25, 23
Tafalla, M., Myers, P. C., Caselli, P., & Walmsley, C. M. 2004, Ap&SS, 292, 347
Taylor, S. D., Morata, O., & Williams, D. A. 1996, A&A, 313, 269
Taylor, S. D., Morata, O., & Williams, D. A. 1998, A&A, 336, 309
Tobin, J. J., Hartmann, L., Looney, L. W., & Chiang, H. F. 2010, ApJ, 712, 1010
Valenti, J. A., Basri, G., & Johns, C. M. 1993, AJ, 106, 2024
Visser, A. E., Richer, J. S., & Chandler, C. J. 2002, AJ, 124, 2756
Vorobyov, E. I., & Basu, S. 2005, ApJ, 633, L137
Vorobyov, E. I., & Basu, S. 2006, ApJ, 650, 956
Weingartner, J. C., & Draine, B. T. 2001, ApJ, 548, 296
Whitney, B. A., Wood, K., Bjorkman, J. E., & Cohen, M. 2003, ApJ, 598, 1079
Young, C. H., & Evans, N. J., II. 2005, ApJ, 627, 293